



FACULTY  
OF SCIENCE

# Design of a Temperature Insensitive Fiber Interferometer for Long-Term Laser Frequency Stabilization using Metal Coated Fibers

Saskia Bondza

---

Thesis submitted for the degree of Master of Science  
Project duration: 8 months, 60 hp

Supervised by Lars Rippe and Alexander Bengtsson

Department of Physics  
Division of Atomic Physics  
May 2019



# Contents

<b>1</b>	<b>Introduction</b>	<b>1</b>
1.1	General Introduction . . . . .	1
1.2	Framework: Medical Imaging . . . . .	2
1.2.1	Narrowband Spectral Filters with Spectral Hole Burning . . . . .	3
1.2.2	Demands on the Laser . . . . .	4
1.3	Microscopic Explanation of Thermal Expansion . . . . .	4
<b>2</b>	<b>Laser Frequency Stabilization using Fiber Interferometry</b>	<b>6</b>
2.1	Operational Principles . . . . .	6
2.1.1	Working Mechanism . . . . .	6
2.1.2	Homodyne and Heterodyne Detection . . . . .	8
2.1.3	Polarization . . . . .	9
2.2	Review . . . . .	10
<b>3</b>	<b>Long-term Laser Frequency Stabilization using a Fiber Interferometer</b>	<b>12</b>
3.1	Temperature Sensitivity . . . . .	12
3.2	A Drift-free Fiber Interferometer . . . . .	14
3.2.1	Detection Scheme . . . . .	14
3.2.2	Polarization Management . . . . .	15
3.2.3	Noise Analysis . . . . .	16
3.3	Special Considerations for the Drift-free Fiber Interferometer . . . . .	17
<b>4</b>	<b>Thermal Sensitivity of Coated Fibers</b>	<b>19</b>
4.1	Overview . . . . .	19
4.2	Thermal Stress . . . . .	21
4.3	Analytic Solution . . . . .	22
4.4	Simulation . . . . .	24
<b>5</b>	<b>Experimental Study</b>	<b>26</b>
5.1	Principle . . . . .	26
5.2	Experimental Set Up . . . . .	28
5.2.1	Design of a Heat box . . . . .	28
5.2.2	Optical Set Up . . . . .	30
5.3	Experimental Procedure . . . . .	32
<b>6</b>	<b>Results</b>	<b>35</b>
6.1	Data Analysis . . . . .	35
6.2	Thermal Sensitivity of Coated Fibers . . . . .	36
6.3	Discussion . . . . .	40
<b>7</b>	<b>Outlook</b>	<b>41</b>
<b>8</b>	<b>Appendix</b>	<b>47</b>

## Acknowledgements

First and foremost I would like to thank my supervisors Alexander Bengtsson and Lars Rippe for the opportunity to do my thesis in the Quantum Information group and their support and guidance. I want to thank Lars in particular for sharing his vast experience and expertise and teaching me independent scientific work and thinking.

I want to thank the people who were not directly involved with my thesis in particular. This includes Sebastian for being the lab wizard of the group and knowing where to find and how to fix almost everything, Åke for helping me out with the electronics and teaching me how to solder, Anders for letting me borrow his power supply and teaching me how to use the milling machine and the rest of the QI group for their input and support and a nice work environment.

I also want to thank the other master students doing their thesis for mutual support and distraction when a break was needed. This includes Robin, Ian, Maitane, Jess, Javier and in particular Armand, Lisa and Shekhar who also carried out their thesis work in Atomic Physics.

Lastly, thanks to everyone who was willing to read my popular description as non-physicists and gave feedback on whether it made sense - thanks Gustav, Ieva, Kristin and Gabby!

## Abbreviations

AOM	Acousto-Optic Modulator
BS	Beam splitter
CTE	Coefficient of Thermal Expansion
EOM	Electric Optical Modulator
FBG	Fiber Bragg Grating
FC	Fiber Coupler
FHWM	Full half width maximum
FM	Faraday Mirror
FPI	Fabry-Pérot Interferometer
MI	Michelson Interferometer
MZI	Mach-Zehnder Interferometer
PID	Proportional–integral–derivative controller
ULE	Ultra-low Expansion
UOT	Ultrasound Optical Tomography
VA	Electrically controlled variable attenuator
VCO	Voltage controlled oscillator

## Abstract

This work presents the design for a temperature drift-free path imbalanced fiber interferometer for long-term laser frequency stabilization using coated fibers with different thermal drift.

For this purpose, single acrylate, dual acrylate, copper and aluminum coated fibers are analyzed theoretically and experimentally regarding the thermal sensitivity of their optical path length. Experimental results were obtained by using few meter sample fibers as low-finesse cavities and measuring the phase of the cavity modes drifting by as a function of temperature. Measurements yield temperature sensitivities of  $9.51 \cdot 10^{-6} \text{ K}^{-1}$ ,  $10.85 \cdot 10^{-6} \text{ K}^{-1}$ ,  $14.59 \cdot 10^{-6} \text{ K}^{-1}$  and  $17.86 \cdot 10^{-6} \text{ K}^{-1}$  for the single acrylate, dual acrylate, copper and aluminum fiber respectively and are in general in good agreement with theoretical results. A suggestion for a custom-made aluminum fiber derived from the presented model with an increased thermal sensitivity of  $28.6 \cdot 10^{-6} \text{ K}^{-1}$  is further presented.

Choosing aluminum coating for the short arm and single acrylate for the long arm of the fiber interferometer with their length ratio corresponding to the ratio of their thermal sensitivity makes the path difference constant with temperature and the interferometer thus drift-free. A trade-off is to be made between the introduced additional delay of the short arm and the obtained path difference. An additional delay puts demands on the pre-stabilized linewidth of the laser while the latter improves short-term linewidth reduction.

# 1 Introduction

## 1.1 General Introduction

Humanity's strive for knowledge and the advances in science and technology arguably started with measurement of time. Thousands of years ago first calendars were developed based on careful observation of the moon, the sun and other stars. As humanity progressed, measurements for time progressed leading to further innovation. In 1364 the first detailed description of a clockwork using mechanical oscillations is presented by Giovanni da Dondi in *II Tractus Astarii* [1]. In the 18th century, hundreds of years later, a precise portable clock made accurate navigation at sea possible illustrating the fundamental function of time measurement in science, technology and engineering. During the industrial revolution clocks then went on to determine our daily life [1].

In the last 100 years a new source of regular oscillations was found in the form of coherent light emitted by a laser. In an interview with the *New York Times* Maiman, who was largely involved in the development of the first laser, stated "a laser is a solution seeking a problem" [2]. Now lasers are of course omnipresent in research and industry with a large variety of applications from medicine to manufacturing and are further the most accurate time measurement currently available in the form of atomic clocks where lasers are stabilized to an atomic transition [3, 4]. As well as the range of applications of lasers, the need in their precision keeps increasing. A lot of efforts and work were focused in the last decades on making lasers more and more stable. Current standard for laser frequency narrowing is using an ultra-low expansion cavity (ULE cavity) as a frequency reference. ULE cavities are made of ultra-low expansion materials that have a zero point of thermal expansion at their operation temperature. With thermal stabilization, active vibration isolation and placement in a vacuum chamber a linewidth on the order of Hertz can be reached [5]. However, this is a very costly procedure. A ULE cavity costs about 100,000 SEK alone and with the necessary isolation one quickly reaches a million SEK. Additionally, this stabilization technique usually only allows operation in a lab unless more efforts and money go into a more mobile set-up [6].

An alternative that has gotten some attention in recent years is the use of fiber interferometers [7]. However, much like reference cavities before the introduction of the ULE material, fiber interferometers have one major weakness: their drift with temperature variations [8]. This work introduces a concept to design a temperature insensitive fiber interferometer using coated fibers eliminating the major drawback this device exhibits. A more robust, low cost and compact solution would open up the use of stabilized lasers in medicine, transportation (e.g. on airplanes) and other applications. Furthermore, with the rise of quantum technology in recent years in industry the need for compact and cheap laser stabilization systems will increase, too.

A main focus of the thesis is given by the analysis of the thermal sensitivity of coated fibers. This is of a large interest in a broader context as optical fibers have a number of industrial applications i.e. in the form of sensors. Fiber-based sensor technologies allow measurements of strain, change in orientation, pressure and temperature [9]. Thermal sensitivity of the optical path length is an important characteristic in these applications as well as all other phase sensitive applications. Additionally, fiber interferometers are used in various applications for measurements, such as distance measurements, so that a drift-free fiber interferometer is of larger interest in numerous applications [10].

## 1.2 Framework: Medical Imaging

The framework of this thesis is the ongoing project in the quantum information group at Lund University in developing a medical imaging technique called Ultrasound Optical Tomography or UOT for short. This technique combines an ultrasonic wave focus with light pulses of a duration of approximately  $1 \mu\text{s}$  to achieve a good penetration depth of about 5 cm while still being able to retrieve spectral information. Ultrasound alone can penetrate tissue almost unperturbed and is a very common medical imaging technique. However, no spectral information can be obtained. Light on the other hand is strongly scattering and can only penetrate tissue on a mm scale before losing all spatial information. It does however convey spectral information. Combination of both is a potential way to solve this problem. Here, the mechanism that is taken advantage of is the Doppler shift. Due to the Doppler shift, photons that are diffracted by the ultrasonic focus are shifted in frequency. Separating the Doppler shifted photons from the original carrier signal thus gives spatial resolution corresponding to the size of the ultrasonic focus [11]. As the shift is on the order of MHz as it corresponds to the frequency of the ultrasound and is thus rather small, sophisticated filtering is required. In this group, a rare earth ion doped crystal is used that can be frequency selectively bleached at the Doppler shifted frequency making the crystal transparent for this wavelength [12]. The functional principle of UOT is depicted in figure 1.

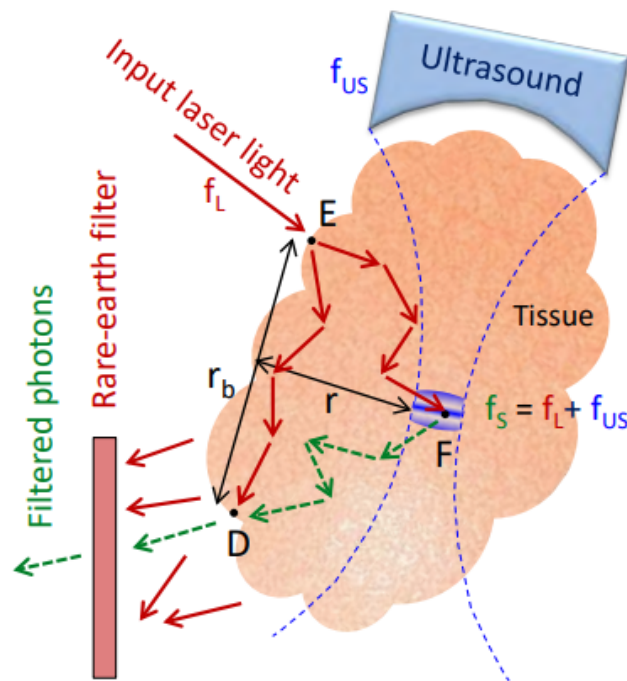


Figure 1: Working Mechanism of Ultrasound Optical Tomography: The combination of ultrasound and light allows deep tissue spectral imaging by taking advantage of the Doppler shift that occurs when light is diffracted by an ultrasound focus. The signal in form of the Doppler shifted photons is filtered out with a rare earth ion doped crystal. The spatial resolution then corresponds to the size of the ultrasound focus. [11]

One aim of the UOT project is to detect the oxygen content of blood in the frontal part of the myocardial tissue. The contrast mechanism for this purpose is the difference in

absorption coefficient - oxygenated and desoxygenated blood have vastly different absorption spectra. The difference is particularly large at a wavelength of around 700 nm while absorption by muscle and other tissue is low making it a suitable working wavelength [11]. A prime application of the UOT technique is the fast diagnosis of heart diseases since they are still one of the leading causes of death worldwide. However, other applications such as the treatment of tumors may also be a possibility.

### 1.2.1 Narrowband Spectral Filters with Spectral Hole Burning

Rare earth ion doped crystals have the characteristic ability to be frequency selectively bleached for a small given frequency range. This process of achieving transparency for a small optical frequency range is called spectral hole burning. Ground state  $A$  of the rare earth ions is depopulated by repeatedly exciting to the energy state  $B$  with the laser frequency  $f_0$  until all electrons are in the metastable state  $C$  as it is illustrated in figure 2 b). If a photon with an energy corresponding to the transition from  $A$  to  $B$  is then incident, it will no longer be absorbed. Due to imperfections in the crystal, different ions will have slightly shifted transitions which is illustrated in form of the green, blue and red rare earth ion in figure 2 a). Burning with a laser will address a class of rare earth ions lying in the frequency range corresponding to the stability of the laser used, here indicated in green, and thus a transmission window is created (see figure 2 c) and d)).

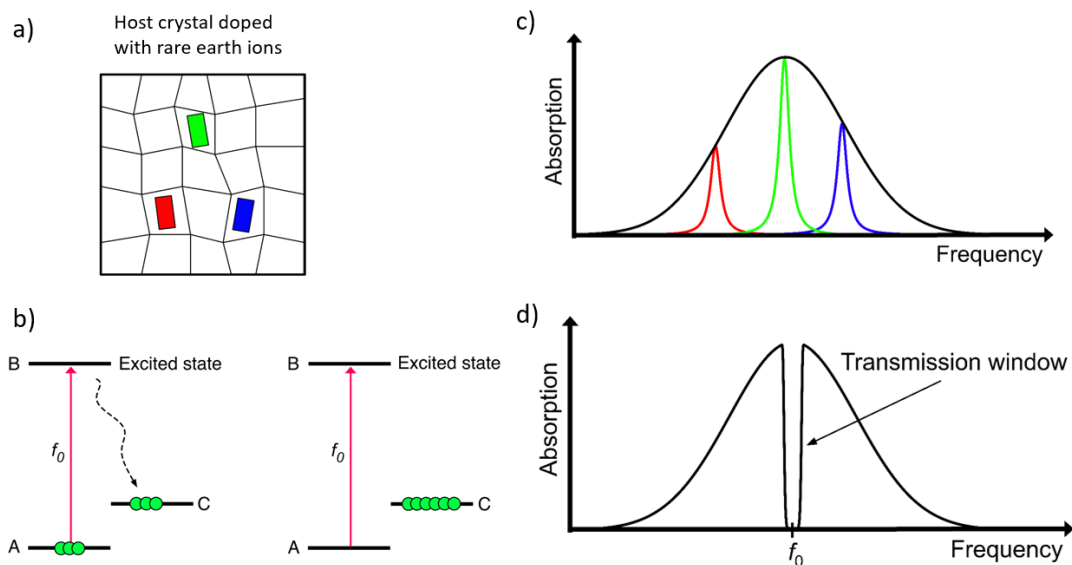


Figure 2: Narrowband Spectral Filters with Spectral Hole Burning: Depopulating the  $A$  to  $B$  transition in a class of ions with transitions in the same narrowband spectral range around  $f_0$  creates a transmission window. Image courtesy of the QI group.

Rare earth ion crystals can only be used at selective frequencies. In this group, it is aspired to use a Thulium-doped crystal with Lanthanum trifluoride as host material. This material can be bleached at a wavelength of 690 nm, which is within a suitable range for imaging of the oxygen content of blood in the frontal part of the myocardial tissue.

Besides the potential as spectral filters, Spectral Hole Burning has gained the most attention for its potential application as frequency domain optical storage. Binary would then be coded with the presence of a spectral hole, a digital 1, or the absence of a spectral

hole, a digital 0. Other potential applications include pulse shaping as well as other forms of optical signal processing [13].

### 1.2.2 Demands on the Laser

In order to obtain a filter with suitable properties using the spectral hole burning technique described above, the laser used in the process must fulfill certain stability requirements. Firstly, to obtain sharp filter edges and thus ensure good frequency discrimination the short-term stability of the laser can not be broader than the linewidth of the ions which is on the order of a few kHz. Secondly, during image acquisition the drift of the laser can not be more than a small fraction of the Doppler shift to avoid the carrier signal drifting towards the Doppler shifted signal frequency the hole was burned at and thus falsifying the intensity sensitive measurements. This is illustrated in figure 3. Consequently, a long-term stability of at least 50 kHz is required.

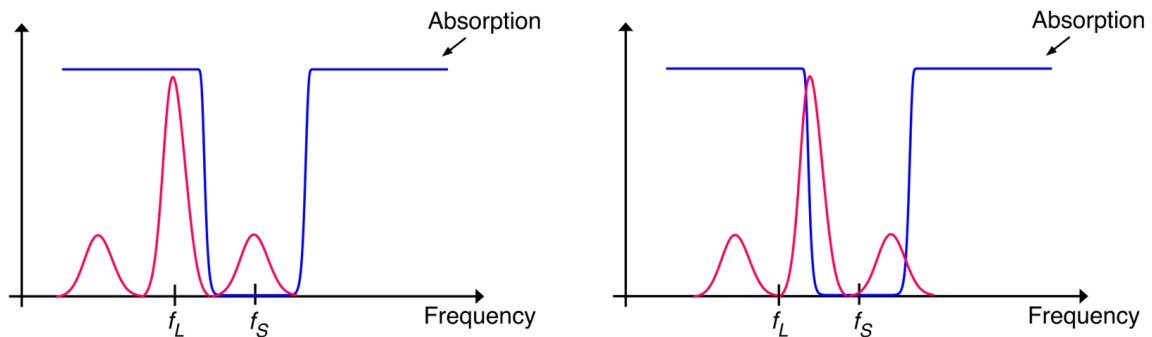


Figure 3: Stability requirements of the laser: In order to obtain sharp edges, a good short-term stability of a few kHz is required. Throughout the image acquisition the laser can not drift more than a small fraction of the Doppler shift i.e. 50 kHz to prevent the carrier signal from leaking through the filter. Image courtesy of Alexander Bengtsson.

A laser with those specifications ( $\approx 5$  kHz short term stability, no more than 50 kHz, wavelength 690 nm) is not readily commercially available. As a result, a decision was made to purchase a laser and build a system to stabilize it further in frequency to meet the demands.

Originally, the aim of the thesis was to build a system as presented in the literature. However, as I started working I identified temperature drift as a main problem and came up with a new design to solve this problem satisfactorily.

## 1.3 Microscopic Explanation of Thermal Expansion

As thermal expansion is one of the key concepts studied in this thesis, a brief simplified, introductory explanation is given in this section.

The potential between two atoms is characterized by opposing attractive and repulsive forces that make bonding possible. Attractive forces result for instance from electric dipole interaction and are necessary to hold atoms in place while repulsive forces are a result of the Coulomb interaction of the outer electrons and make sure atoms do not get too close to each other [14]. Many characteristics can be derived from a harmonic

approximation but the resulting potential is in fact asymmetric. A simple model for an interatomic potential  $\Phi$  is the Lennard-Jones potential given as  $\Phi(r) = \frac{A}{r^n} - \frac{B}{r^m}$ , where  $r$  is the distance between two atoms and  $n, m$  denote integers while  $A$  and  $B$  are positive constants [14]. Such a potential is plotted in figure 4 where  $n = 6$  and  $m = 1$ .

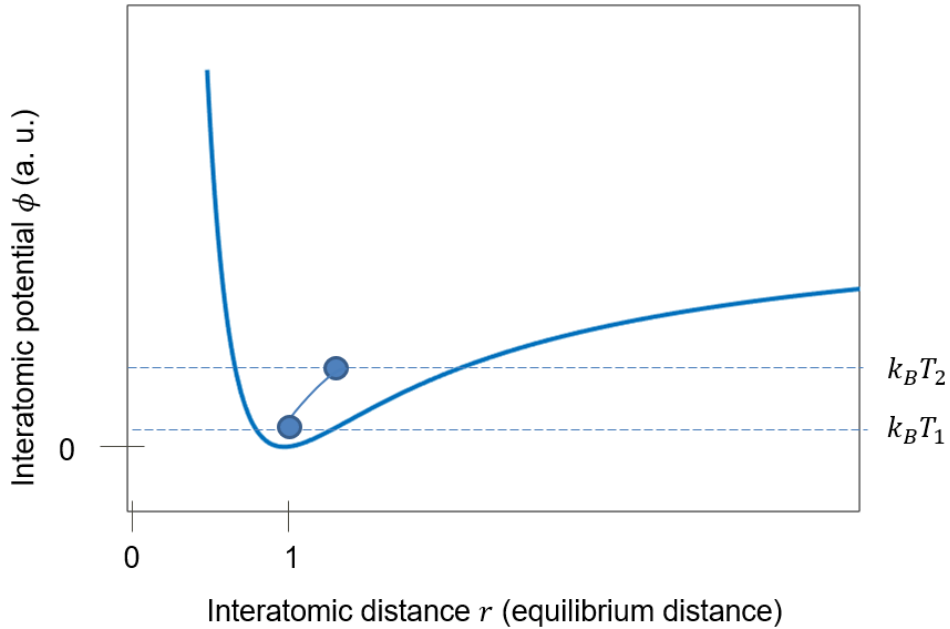


Figure 4: Microscopic Explanation of Thermal Expansion. An atoms average distance increases with its energy and thus with its temperature due to the asymmetry of the interatomic potential. Figure adapted from Hoffman, Solid State Physics [14].

Following statistical mechanics, the atom has an average energy of  $k_B T$ , where  $T$  is its temperature. This is also referred to as the equipartition theorem. Let us consider an atom with a low temperature  $T_1$  as depicted in figure 4. As this corresponds to a low energy little above the minimum, the harmonic approximation of the potential holds: the atom can move equally far left and right of the minimum of the potential resulting in an average position corresponding to equilibrium distance. However, with an increased temperature  $T_2$ , the asymmetry of the potential starts to effect the problem and an atom with an average energy of  $k_B T_2$  can move further away than it can approach the atom seen from equilibrium distance. This means that its average position and thus distance from each other will increase [14]. Looking at a larger ensemble of atoms this is what then causes call thermal expansion with

$$\frac{\Delta l}{l} = \alpha \Delta T \quad (1)$$

where  $l$  is the length of the material,  $\Delta l$  the resulting length change of the temperature change  $\Delta T$  and the coefficient  $\alpha$  is referred to as the linear coefficient of thermal expansion (CET). The CET itself is of course temperature dependent and approximated as constant for sufficiently small  $\Delta T$ . As intuition suggests,  $\alpha$  approaches 0 close to  $T = 0$  K [14].

## 2 Laser Frequency Stabilization using Fiber Interferometry

The principle behind laser stabilization using a path imbalanced fiber interferometer is rather simple. Due to a path difference in the arms, the laser output at a time  $t$  is compared to the laser output at an earlier time  $t - \tau$  where  $\tau$  is the delay induced by the optical path difference. Changes in frequency will generate an error signal that is fed back to the laser. The following section will give a more detailed description of this mechanism as well as a brief review of literature on this matter.

### 2.1 Operational Principles

#### 2.1.1 Working Mechanism

A fiber interferometer for laser frequency stabilization can be thought of as a frequency-to-phase converter as described by Chen *et al.* [15]. A simplified set up to illustrate the working mechanism is given in figure 5. The fiber interferometer consists of two arms of lengths  $L_1$  and  $L_2$  with  $L_2 > L_1$  which introduces the delay  $\tau$  to the beam propagating through the longer arm with respect to the shorter arm given as

$$\tau = \tau_2 - \tau_1 = \frac{nL_2}{c} - \frac{nL_1}{c} = \frac{nL}{c} \quad (2)$$

where we have introduced the path imbalance  $L = L_2 - L_1$  and  $n$  denotes the refractive index of the fiber with  $c$  denoting the speed of light in vacuum.

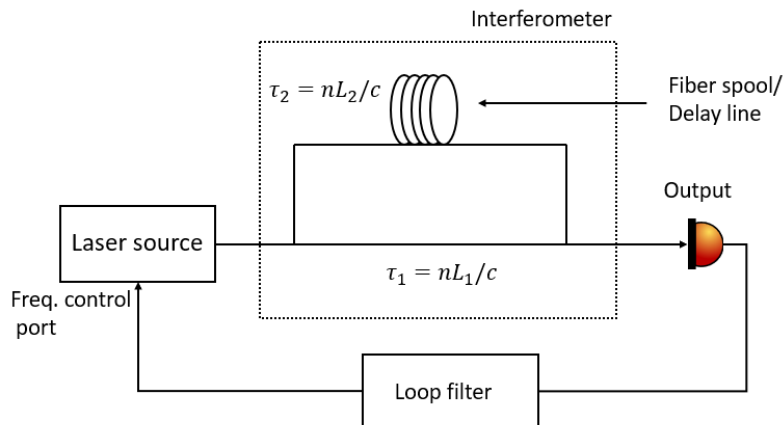


Figure 5: Working Mechanism of Laser Stabilization with a fiber interferometer. Figure adapted from Jiang [7]

The electric fields in the arms of the fiber interferometer directly before recombination yield:

$$E_1 = E_0 \sin [(\omega t) + \Gamma \sin (\Omega t)] \quad (3)$$

$$E_2 = E_0 \sin (\omega'(t + \tau)) \quad (4)$$

where  $\omega$  and  $\omega'$  denote the angular frequency of the beam in each arm of the interferometer and  $\Gamma$  and  $\Omega$  denote fluctuations on amplitude and frequency. For two coherent interfering beams the intensity after recombining both beams is given as  $I = |(E_1 + E_2)|^2$ . For the power output produced by a detector assuming that high frequency components are filtered out and rewriting  $E_1$  using the Bessel series approximation (see Chen *et al.* [15]) this then yields:

$$P(t) \approx -E_0^2 \Gamma \sin \left[ (\omega - \omega')t - 2\pi \frac{nL}{\lambda'} \right] \quad (5)$$

$$(6)$$

This is the produced error signal and phase locking can then achieve frequency stabilization in the following way:

$$\sin \left[ (\omega - \omega')t - 2\pi \frac{nL}{\lambda'} \right] = 0 \quad (7)$$

$$\longrightarrow (\omega - \omega')t = 0 \quad (8)$$

$$2\pi \frac{nL}{\lambda'} = N\pi \text{ N is an integer} \quad (9)$$

which keeps the difference between the frequencies in both arms at 0 which due to the delay introduced then of course corresponds to  $\omega(t) = \omega(t + \tau)$  resulting in a constant frequency over time thus stabilizing the laser. This analysis assumes a constant path difference between both fibers which requires appropriate isolation from temperature fluctuations and other environmental noise. For a more detailed discussion please refer to sections 3.1 and 3.2.3. The error signal is fed back to a unit of the laser controlling the frequency. In the case of a diode laser this can be as simple as feeding back to the power supply or take more complex forms such as feeding back to an electro-optic modulator (EOM) that has been placed in the laser cavity for the purpose of laser stabilization. Crucial is that the feedback happens at a high frequency making i.e. acousto optic modulators (AOMs) less suitable in most cases due to their inherent delay.

One can further define the quality factor  $Q$  as follows:

$$Q = f_0 \frac{\partial \phi}{\partial f_0} = 2\pi f_0 \tau \text{ [rad/Hz]} \quad (10)$$

so that the frequency discrimination slope for the frequency  $f_0$  the laser is stabilized is given as  $2\pi\tau = 2\pi \frac{nL}{c}$  [7]. This means the larger the path imbalance the better frequency discrimination is achieved and the narrower the stabilized linewidth of the laser will be as a result. Note that derivation here is carried out for a Mach-Zehnder interferometer (MZI) but holds up equally for a Michelson interferometer (MI) with the only difference being of course that an equivalent MI has fibers with half the physical length as light propagates to the mirrors and back.

### 2.1.2 Homodyne and Heterodyne Detection

Fiber Interferometers for laser frequency stabilization require a detecting scheme that will be insensitive to intensity fluctuations of the laser as otherwise an intensity fluctuation of the laser could falsely be interpreted as a phase change caused by a shift in frequency. For laser frequency stabilization using fiber interferometry two different options are worth considering and shall be discussed in the following. These two techniques are balanced homodyne detection and heterodyne detection.

**Homodyne Detection** Balanced homodyne detection is a detection technique where the interference signal is detected twice and the measured intensities are then subtracted from each other which eliminates any fluctuations in the signal that are due to intensity fluctuations of the laser as those would equally effect both signals and subtract to 1 (assuming an equal splitting ratio). Given that phase difference and polarization are controlled in a suitable manner, we can observe destructive and constructive interference (overall of course conserving the total power) at the two output ports of a fiber coupler according to couple-mode theory [16]. We illustrate this in figure 6 where the blue graph indicates the output power of port 1 and the red graph represents the output power of port 2. We include the detected power in yellow where we subtract both graphs as it is done with balanced detection. The locking point will be chosen as indicated in black.

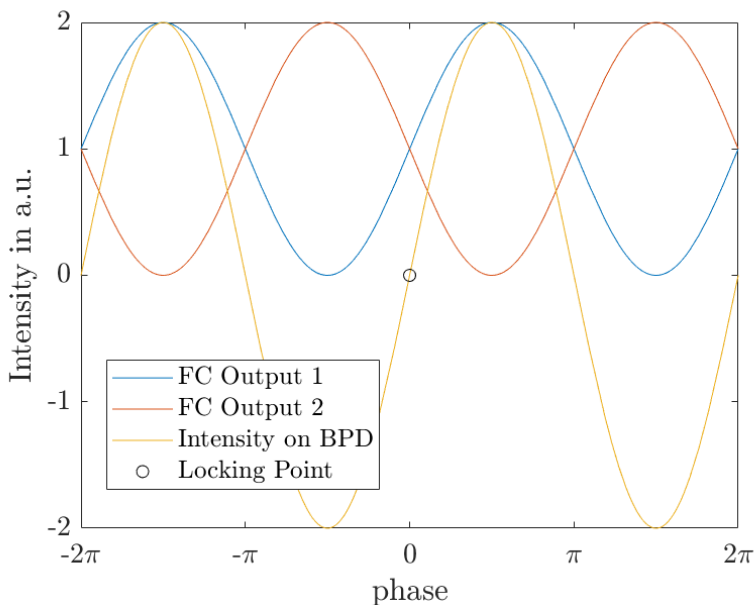


Figure 6: Illustration of the Locking Point of a fiber interferometer in the case of balanced homodyne detection. FC - Fiber Coupler, BPD - Balanced Photodetector

This is favourable for two reasons. Firstly, the magnitude of the derivative reaches its maximum here and thus changes in frequency will lead to a maximum variation in signal. Secondly, setting the zero-crossing as locking point makes it particularly easy to generate the error signal. This choice of locking point further fulfills the quadrature condition ( $I/2$ ) allowing easy derivation of the phase and thus phase-locking [17].

**Heterodyne Detection** Heterodyne detection employs an AOM in one of the arms of the interferometer shifting the frequency of light propagating in that arm by  $f_{AOM}$ . Following the derivation carried out in section 2.1.1, the power output produced by a detector after filtering and demodulation hence yields the beat note signal

$$P(t) \propto \sin \left[ (\omega - \omega' + f_{AOM})t - 2\pi \frac{nL}{\lambda'} \right] \quad (11)$$

This is compared with a reference signal with the same frequency as the frequency  $f_{AOM}$  the AOM is driven with finally producing the following error signal:

$$\sin \left[ \left( \underbrace{\omega - \omega' + f_{AOM}}_{\text{frequency output from the FI}} - \underbrace{f_{AOM}}_{\text{reference}} \right) t - 2\pi \frac{nL}{\lambda'} \right] \quad (12)$$

Thus effectively leading to similar locking scheme where the difference between the reference and the frequency output from the FI is kept at 0 from which  $\omega - \omega' = 0$  follows. The main advantage of heterodyne detection is that the error signal is produced by mixing with a reference and is thus truly insensitive, solely the difference in frequency between the interferometer output and the reference is critical. Heterodyne detection is often claimed to give improved stability over homodyne locking [7, 17] as it is more robust. Homodyne locking has a certain calibration dependency.

### 2.1.3 Polarization

Optical fibers can in practice never be manufactured perfectly and always experience a certain degree of birefringence and thus do not preserve polarization. This becomes an issue as the intensity of two interfering beams is dependent on the angle of polarization  $\delta$  between them the same way it depends on the phase between both:  $I = I_0 \cos \delta$ . There exist different ways to control the polarization. For fiber interferometers usually polarization controllers are used with a Mach-Zehnder interferometer and Faraday mirrors (FM) with a Michelson interferometer. A more detailed discussion is given in section 3.2.2.

## 2.2 Review

Fiber interferometers for short term laser stabilization have been realized by a number of groups as alternative to expensive, bulky and sensitive stabilization to a cavity. As pointed out in the previous section, stabilizing to a fiber interferometer requires the assumption that the path difference is constant to be valid and imposes a high importance on efforts regarding isolation or other ways to suppress noise. Efforts in designs established already, range from simple isolation schemes with a Styrofoam box to very sophisticated schemes involving filtering with the help of a second interferometer [17–19].

The aim of this section is to give a brief overview of the different design that have been implemented thus far as well as to quantify their efficiency. For this purpose, table 1 summarizes essential information from the papers at hand giving information regarding the linewidth pre- and post stabilization, path imbalance and information regarding their isolation schemes. A good measure of quantifying how good different interferometers work as a frequency-to-phase converter is to look at how sensitive they detect intensity fluctuations. This can be derived from the path imbalance  $L$  and linewidth  $\Delta f$  in the following way:

$$I = I_0 \cos(\Delta\phi) = \cos\left(\frac{2\pi\Delta f n L}{c}\right) \quad (13)$$

$$res = \cos\frac{\pi}{2} - \cos\left(\frac{\pi}{2} + \Delta\phi\right) \quad (14)$$

where  $res$  denotes resolution indicating what relative intensity changes  $res = \frac{\Delta I}{I}$  can be detected. This information is further added in table 1.

One of the simplest schemes is established by Lee et al.. Their design consists of a fiber interferometer with a path imbalance of 5 m to stabilize a laser with an initial linewidth of 3 MHz. It consists of a Mach-Zehnder interferometer and a balanced detection scheme. The feedback is provided in form of current feedback to the laser [17].

Kéfélian et al. based there design instead on a Michelson interferometer using Faraday mirrors with heterodyne detection and a much longer delay line of 2 km. They further invest in a more complex isolation system [18]. Jiang is from the same group and thus presents a similar design in his PhD thesis, but with more advanced electronics [7].

An interesting variation on the standard stabilization scheme is presented by Lintz et al. in the form of a feed forward system contrasting the standard feedback systems [20].

The most advanced scheme is presented by Dawei et al. in the form of two interferometers with advanced filtering in an attempt to separate environmental noise from frequency fluctuations. While very good results are obtained with this set-up it has a complexity that does not provide the advantages of compactness, transportability and robustness pointed out previously [19]. Smid et al. present a MI with a path imbalance of 2.09 km using heterodyne detection with a slow feedback loop to their laser module and a fast feedback to an AOM placed in front of the fiber interferometer [21]. Finally, Kong et al. present a scheme for long-term laser stabilization that we will discuss in detail in section 3.1 [8].

Paper	Unstabilized laser linewidth	Stabilized laser linewidth	$\Delta L$	Intensity sensitivity $\Delta I/I$	Isolation	Comments
Lee <i>et al.</i> [17]	3 MHz	15 kHz	5 m	0.0023	Aluminum box with 4 mm thick walls, temperature stabilization at 25°C with thermo-electric cooler, Styrofoam box surrounding aluminum box	simple set-up with A MZI
Kéfélian <i>et al.</i> [18]	10 kHz	1 Hz	2 km	0.0001	Fiber spool placed into ring-shaped aluminum box, interferometer placed inside a thick aluminum box with thermo-isolating thermo-plastic film, set onto vibration isolation platform, everything put into acousto-isolating box	
Jiang	$\approx$ 20 kHz	2 Hz	2 km	0.0001	Spool placed in toroidal shaped aluminium box, place entire interferometer in aluminum box with thermal isolation (Myler) $\rightarrow$ put on passive vibration isolation platform	same group as Kéfélian
Lintz <i>et al.</i> [20]	3 MHz	4 kHz	3 m	0.0004	Active thermal stabilization of the laser	Feed forward system with 20m delay line to correct for electronic delays
Dawei <i>et al.</i> [19]	10 kHz	40 mHz	10 km	$10^{-6}$	Active temperature stabilization by filtered feedback to the AOM	Two complex interferometers, not suitable for the desired application
Smid <i>et al.</i> [21]	1.5 kHz	330 Hz	2.09 km	0.02	Set up placed in concrete box that was placed in wooden box to isolate from air fluctuations etc., placed in stable box to isolate from acoustic and seismic vibrations	slow feedback to laser module, fast feedback to AOM
Kong <i>et al.</i> [8]	DFB Laser $\approx$ MHz	32 kHz at 10 s, 754 kHz at 5000 s	5 m	$\approx$ 0.001	Two interferometers, one a lot more temperature sensitive feeding back to temperature controller, thermal isolating box	aiming specifically at long-term stabilization

Table 1: Review of different Fiber Interferometers for Laser Frequency Stabilization

From equation 13 and 14 we can derive the achievable linewidth as a function of path imbalance for given intensity sensitivities  $\Delta I/I$ . In figure 7 we plot the obtainable short-term stability as a function of path difference for intensity sensitivities of 1 in 10 000, 1 in 1000 and 2 in 1000. As a result of the review carried out, a intensity sensitivity of 0.001 – 0.002 seems reachable with reasonable passive isolation. The aim is a short-term stability of few kHz. This aim should be reached comfortably with a path difference of around 40 m, an estimation that includes a certain buffer. For reference, 5 kHz are indicated in form of a dotted black line.

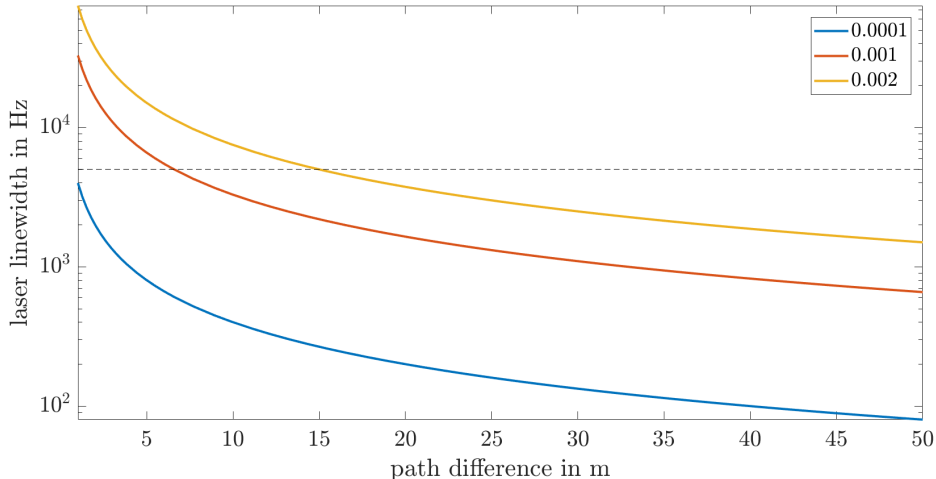


Figure 7: Achievable linewidth as a function of path imbalance of a fiber interferometer for laser stabilization considering different achievable intensity sensitivities

### 3 Long-term Laser Frequency Stabilization using a Fiber Interferometer

As pointed out previously, a clear differentiation is to be made between short and long term laser frequency stability or linewidth and drift. While estimations for a design fulfilling criteria (see section 1.2.2) of a desired short term stability can easily be made from a literature review as presented in the previous section, little work has been carried out regarding long term laser frequency stabilization using fiber interferometry. The following section is result of my considerations and presents a new approach for long term laser frequency stabilization using fiber interferometry.

#### 3.1 Temperature Sensitivity

Already one of the earliest papers published on laser stabilization using interferometers in 1989 by Chen *et al.* pointed out mechanical thermal noise as a potentially seriously limiting factor [15]. This is even more true when considering the laser drift over longer time scales. While silica glass, the material fiber core and cladding are commonly made of, has a relatively low thermal expansion coefficient of  $0.5 \cdot 10^{-6} \text{ K}^{-1}$  the thermo-optic coefficient describing the thermal sensitivity of the refractive index of a material is given as  $\frac{dn}{dT} = 9.1 \cdot 10^{-6} \text{ K}^{-1}$ . For bare fiber this gives an overall thermal sensitivity of the optical path length of  $9.6 \cdot 10^{-6} \text{ K}^{-1}$ .

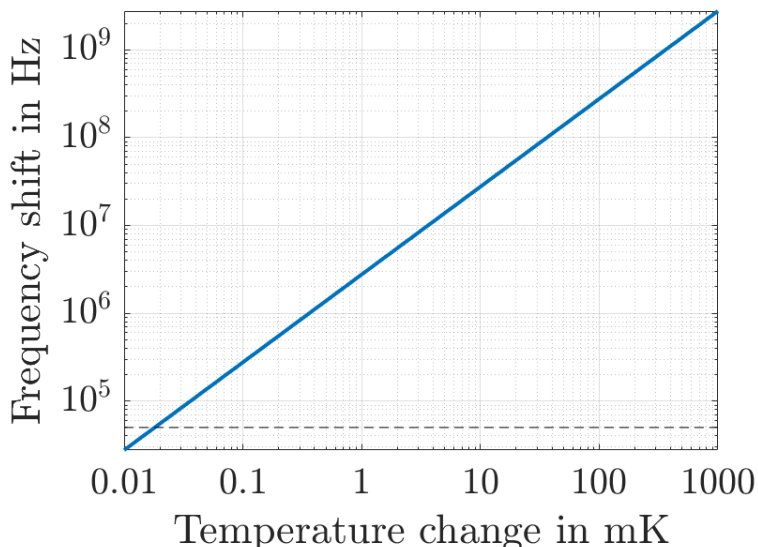


Figure 8: Temperature Sensitivity of fiber interferometers. Both frequency shifts and temperature fluctuations cause a phase shift. The plot shows frequency shifts and temperature fluctuations causing the same shift in phase: A shift of 2 mK causes the same phase shift as a frequency shift of 5 MHz. This couples the achievable sensitivity to the achievable temperature stability.

As we have discussed previously the fiber interferometer can be considered as a frequency-to-phase converter so that we can analyze the derivatives of phase with respect to frequency and temperature to compare the sensitivity of the fiber interferometer regarding both quantities and derive resulting limitations quantitatively. The result of this analysis is presented in figure 8. The plot shows frequency change as function of temperature change that are translated into the same phase shift by a fiber interferometer. While not entirely obvious at first this relation is not dependent on the path imbalance of the fiber interferometer as this comes into play for both effects and thus cancels out. As we can see the influence of temperature fluctuations is drastic. Temperature stability on the sub-mK scale is necessary to obtain a stability in the kHz range. A temperature drift of 0.02 mK corresponds to a frequency shift of 50 kHz.

An interesting approach for long-term stabilization dealing with this problem is presented by Kong *et al.*. They suggest a set-up consisting of two interferometers. One interferometer serves as the regular frequency-to-phase converter that feeds back to stabilize the laser. The second interferometer serves instead as a temperature-to-phase converter feeding back to the active temperature stabilization system. Both delay lines of the longer arms of each interferometer are wrapped around an aluminum cylinder. While the delay line of the first interferometer consists of a jacketed fiber, the delay line of the second interferometer is a bare fiber. This means that expansion and contraction of the aluminum cylinder due to thermal fluctuations will not impact the first interferometer but increase the temperature sensitivity of the second as it stretches the fiber inducing an additional elasto-optic effect i.e. a change of refractive index due to mechanical stress [8] (see section 4.2). Effectively, this design adds a fiber interferometer acting as a thermometer to keep the temperature stable on a long-term scale. It is particular effective as it measures the

temperature exactly where the laser interferometer for frequency stabilization is and is more sensitive than any commercially available thermometer. The efficiency is reflected in the achieved stability (see table 1, Kong *et al.*).

However several concerns can be raised here. Firstly, we still observe an increased drift over time in the data provided by the authors hinting at flaws in the design. Secondly, an aluminum cylinder has a much larger thermal mass than optical fibers which should lead to time delay imbalance in the response of the temperature stabilization possible leading to the increased drift mentioned under point one. Lastly, with two interferometers and active temperature stabilization this set-up is still of relatively high complexity and limited portability. These issues are addressed in the new design suggested in the next section and throughout this thesis.

## 3.2 A Drift-free Fiber Interferometer

An obvious alternative to the use of an aluminum spool to achieve a fiber delay line with a different temperature sensitivity as presented by Kong *et al.* is the use of an optical fiber with an intrinsically different thermal sensitivity. This would match a normal optical fiber well regarding thermal time constant. Given such a fiber can be found an additional thought arises: Why not get rid of the thermal sensitivity all together by building a single fiber interferometer that is insensitive to temperature fluctuations. This can be achieved by matching the length ratio of short and long arm to the ratio of the thermal coefficients of the fibers used in those two arms. In other words, one could think of using a double as temperature sensitive fiber for a half as long interferometer arm meaning that the path difference between both arms will stay constant no matter the ambient temperature. This would mean a laser stabilized to this interferometer could effectively be free of thermal drift.

The immediate question is of course what fibers would be suitable. Polymer-based fibers and hollow core fibers were quickly ruled out as they are not truly single mode and commercial availability is limited. Metal coated fibers have already shown to increase the sensitivity of fiber Bragg grating (FBG) based sensors [22] and are thus an excellent candidate for fibers with an increased thermal sensitivity. The fourth chapter of this thesis is solely dedicated to their theoretical analysis while the fifth chapter explores their experimental analysis.

### 3.2.1 Detection Scheme

As discussed previously (see section 2.1.2) balanced homodyne detection and heterodyne detection are the two options for derivation of an error signal insensitive to intensity fluctuations. While heterodyne detection was discussed to be in general favourable, additional considerations have to be made here. While fiber-coupled AOMs are commercially available they do inhabit air spaces of a few mm to cm with an unknown temperature sensitivity of the crystals used. As the aim is to design a drift free fiber interferometer, this would give rise to an unknown offset and introduce a larger thermal weight. Consequently, calibration of the interferometer to be drift-free would be complicated significantly. Furthermore, an AOM and the required electronics increase the complexity of the set up that we aim to keep as simple as possible. It is thus straightforward to design the suggested drift-free interferometer with a balanced homodyne detection scheme.

As pointed out by Hobbs, it is crucial that operations such as subtraction of two signals happens as close to the detection as possible [23]. Balanced detectors that handle detection as well as subtraction of a signal are available and a suitable, compact option. However, it needs to be noted that the discussion so far has assumed equal power on both inputs of the balanced detector which is not trivial to achieve. A first difficulty is given by the fact that commercially available fiber couplers have an uncertainty of up to 6% on the output ratio. Higher losses in the long arm will lead to further discrepancies. A solution to this problem is including an electronically controllable fiber-coupled variable attenuator that is placed after the fiber interferometer and does thus not interfere in the frequency-to-phase conversion. Another way to solve this would be the use of a balanced detector with a variable current splitter similar to the design presented in "Ultrasensitive laser measurement without tears" [24]. In this case the servo amplifier would be substituted with an adjustable DC voltage, preferably a digital to analog converter, which could be adjusted by introducing a sinus amplitude variation on the input on purpose, and adjust until it is eliminated [25].

### 3.2.2 Polarization Management

As mentioned previously, there are different methods for polarization management in fiber optics available. An overview and a discussion of the three options to consider is given in the following with a conclusion on the best option in the given design context. A first option is polarization-maintaining fibers that exhibit a strong birefringence preserving the eigenmodes of polarization. However, they do exhibit several problems making them less suitable for laser stabilization with a fiber interferometer. For instance, they are very sensitive to alignment and require all components to be polarization maintaining. Their birefringence is temperature dependent meaning they have a high polarization drift with temperature and their polarization axis can wander  $\pm 6^\circ$  [23].

More suitable options for polarization control in the given case are presented by polarization controllers or Faraday mirrors. Polarization controllers make use of the birefringence of fibers induced when being bend or coiled. They are a mechanic device allowing to achieve any desired output polarization for any given input polarization by adjusting angle and coiling of the fiber with the device (for a full explanation see e.g. Saleh and Teich [16]). The downside of this solution is that it requires realignment and thus in order to operate for longer periods of time automatic control of the polarization controller is required.

The most elegant solution for polarization control not requiring realignment is for sure the use of Faraday mirrors. Their use requires a Michelson interferometer. They consist of a Faraday rotator that employ the Faraday effect to achieve a  $45^\circ$  rotation of polarization and a mirror. Upon reflection of the mirror they pass the Faraday rotator a second time resulting in an overall rotation of  $90^\circ$ . While are available with a relatively low temperature dependency ( $0.5^\circ$  change for  $\approx 40^\circ C$  change in temperature) of the rotation angle, Faraday mirrors are in generally narrow band and only perform well for a 20 nm spectrum at best [26]. This swaps the incident polarization components so that on the way back they experience the opposite birefringence effect cancelling each other to 0. The result is a very robust polarization control and has recently been shown to also improve the performance of some fiber sensor applications [27].

The downside of this technique in the discussed frame of a drift free fiber interferometer

is the introduction of free space components. As Faraday mirrors are introduced in both arms optical path changes of the Faraday mirrors due to environmental effects cancel each other to first order. A back-of-the-envelope calculation can be made considering only the thermal expansion of the housing only and gives acceptable results. However, Faraday mirrors need to be custom made for a wavelength of 690 nm and are larger due to the properties of the crystals used. The exact size could not be specified when a quote for a custom-made mirror was provided. Lastly, a Michelson interferometer uses fibers only half as long to achieve the same path difference as a Mach-Zehnder interferometer making the relative precision requirements on the length more demanding and increasing intrinsic noise.

In summary a polarization controller is recommended for wavelengths in the visible range and short path imbalances of a few meters when realignment is acceptable while Faraday mirrors are believed to be the more robust solution for larger path imbalances and in particular for stabilization at wavelengths in the infrared.

### 3.2.3 Noise Analysis

This section is orientated on similar discussion carried out by Jiang [7].

As in a well-working laser stabilization system frequency noise is replaced with measurement noise from the stabilization a brief discussion of noise can not be neglected. We differentiate between intrinsic noise of the optical fibers and environmental noise.

**Intrinsic Noise** Intrinsic noise of the optical fibers is caused by random thermal fluctuations in the optical fiber itself impacting the physical length of the fiber as well as the refractive index. These effects are well understood and give the following phase noise with  $k_B$  denoting Boltzmann's constant,  $l$  the length of the fiber,  $D_{th}$  gives the thermal diffusivity and further  $\kappa$  denotes the thermal conductivity,  $k_{min}$  and  $k_{max}$  are boundary conditions [7]:

$$\phi(f^2) = \frac{2\pi k_B T^2 l}{\kappa \lambda^2} \left( \frac{dn}{dT} + n\alpha_L \right) \cdot \ln \left[ \frac{k_{max}^4 + \frac{2\pi f^2}{D_{th}}}{k_{min}^4 + \frac{2\pi f^2}{D_{th}}} \right] \quad S_{thermal}(f) = \left[ \frac{\phi(f)}{2\pi\tau} \right] \quad (15)$$

Results of this calculation for different fiber lengths are presented in figure 9 and normalized with the noise bandwidth. As already visible from the equation the effect goes down significantly with length. From figure 9 we can further estimate the noise bandwidth to be about 360 Hz giving  $\sqrt{NoiseBandwidth} \approx 60 \sqrt{\text{Hz}}$ . From this, for a fiber length of 5 m a noise level of 600 Hz is estimated while for 20 m and 40 m this drops to 280 Hz and 140 Hz respectively for short time scales. Longer integration times lead to high frequency noise to average out and thus reduced the noise bandwidth.

For a stability goal of kHz this noise will not be a limiting factor. We can see though that ultra-stable lasers on a Hz level require several hundred meters of fiber length as we have seen in the review where 2 km delay lines were used to gain a stability of 1 Hz.

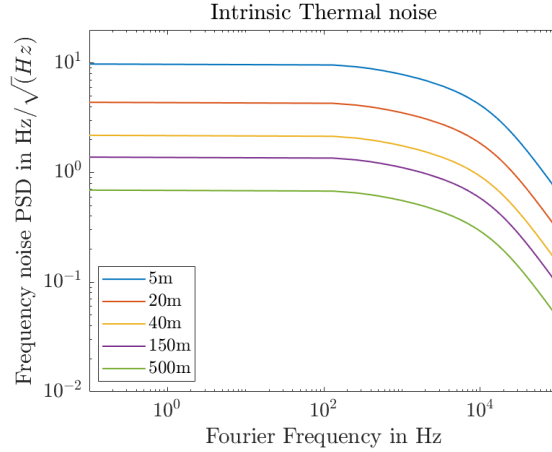


Figure 9: Intrinsic thermal noise of an optical fiber for different lengths  $l$

**Environmental Noise** Environmental noise in the form of vibrations, air fluctuations, acoustic noise as well as temperature fluctuations are the major noise sources impacting fiber interferometers. While the latter is less of a concern in this case, all of these sources can be managed well with passive isolation. As we have seen in table 1 a good approach is the use of two boxes with appropriate insulation materials to decrease air fluctuations, acoustic noise and temperature fluctuations. Where vibrational noise becomes a large issue, a isolation platform can be used. A passive isolation platform is sufficient.

### 3.3 Special Considerations for the Drift-free Fiber Interferometer

Two concerns come to mind when discussing this idea that need to be addressed: 1) The suggested drift-free fiber interferometer requires a longer "short" arm as it has to correspond to the ratio of thermal coefficients. This induces an additional delay in the feedback loop and has larger implications on what properties a laser must have prestabilized - an important result for the laser purchase process of the group 2) An interferometer like this requires precise measurement of both the fiber length as well as their thermal sensitivity.

#### Control Bandwidth

The response time of the feedback system determines the highest frequency of noise that can still be suppressed. Random noise that is at a higher frequency and thus faster than the response time can not be corrected for. This cut-off frequency is known as the unity gain frequency, i.e. the frequency where the suppression ratio is 1, and is dictated by the delays in the system. The frequency bandwidth of noise that can be suppressed is then also referred to as the control bandwidth. The control bandwidth is antiproportional to the delay time of the system i.e. the delay of the feedback loop.

In the case of laser frequency stabilization a rule of thumb to calculate the unity gain frequency is that the product of delay time  $T$  and angular frequency  $\omega$  can not be larger than  $\frac{\pi}{2}$ .

Introducing an additional delay of by increasing the length of the short interferometer arm from 1 m to 20 m in a Michelson set-up in order to achieve the desired path difference

of up to 40 m while having the possibility to choose the lengths of the arms corresponding to a thermal sensitivity ratio that is between 1.5 and 2 reduces the unity gain frequency to 550 kHz where additional electronic delays are taken into account.

In general, this comes down to a trade-off. As the arm lengths are chosen in a set ratio corresponding to the ratio of thermal sensitivity an increase of optical path difference is not possible without an increase in delay imposing higher restrictions on the frequency noise spectrum of the laser prestabilization. As the gain where the frequency of the noise spectrum of the laser before stabilization flattens out should be sufficiently large, the cut-off should be chosen significantly lower than the unity gain frequency e.g.  $\approx 100$  kHz.

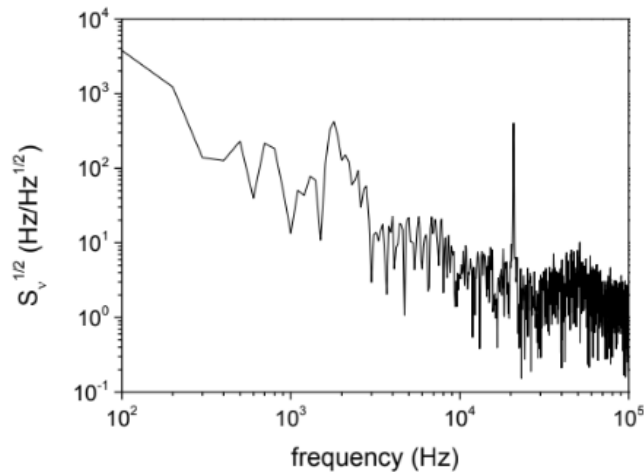


Figure 10: Frequency noise spectrum of the purchased laser: Root power spectral density of frequency fluctuations. [28]

This analysis I carried out presented a major guideline in the laser chosen for purchase that will be stabilized with my design and will arrive in May 2019. As we can see from figure 10 the frequency noise spectrum does indeed flatten out around 100 kHz. A more technical discussion of this problem can be found in the Appendix (see section 8).

### Measurement Precision Requirements

A crucial part in analyzing if building a drift free interferometer in the way suggested is feasible lies in calculating the precision requirements imposed on the fiber lengths and the thermal coefficients as a truly drift free fiber interferometer is only given with perfect experimental precision. This obviously strongly depends on the assumed temperature stability of the environment and the linewidth and drift aimed for. Here, I assume that achieving a long term stability of 0.01 K is easily doable with passive isolation in the form of boxes only. For a short-term stability of 5 kHz and a long-term stability of 50 kHz we then find a maximal acceptable relative error of 0.1%. For a fiber of several meters length this results in a required precision of cm which is feasible. More challenging is the measurement of the thermal coefficients to this precision. It should be noted that the precision of 0.1% applies to the ratio of both thermal coefficients. The relationship between desired long-term stability and required precision is further anti proportional so that for a drift of no more than 25 kHz for instance a precision of 0.05% is required.

## 4 Thermal Sensitivity of Coated Fibers

After having discussed the potential of using optical fibers with different thermal sensitivities for long-term laser frequency stabilization, this section explores the thermal sensitivity of coated optical fibers theoretically giving an analytic as well as a simulation-based analysis of the problem.

### 4.1 Overview

Different coatings for optical fibers have been developed to optimize them for the vast amount of applications they have. While most of the time the coating acts as a protection for certain environmental conditions, such as high temperature resistance or chemical resistance, in particular metal coatings have a potential in altering the thermal characteristics of an optical fiber as well. As the coating and the fiber have different coefficients of thermal expansion (CTE)  $\alpha$ , the fiber experiences thermal stress upon a change in ambient temperature in both axial and radial direction. This has two main effects.

First, the physical length of the fiber changes in a different manner as deformation takes place and secondly the induced stress has an impact on the refractive index of the core and hence further alters the optical length of the fiber. The process depends on the following physical and mechanical quantities: the thickness of core, cladding and coating, Young's modulus  $E$  (sometimes also referred to as elastic modulus in the literature) as well as the Poisson ratio  $\rho$  and lastly the thermal expansion coefficient  $\alpha$  of core, cladding and coating.

To further calculate how the stress generated will impact the thermal behaviour of the

Material	$E/\text{GPa}$	$\rho$	$\alpha/\text{K}^{-1}$	thickness $r$
Silica Glass (cladding)	72.5	0.155	$0.5 \cdot 10^{-6}$	125 $\mu\text{m}$
Aluminum coating	69	0.345	$23 \cdot 10^{-6}$	165 $\mu\text{m}$
Copper coating	117	0.330	$17 \cdot 10^{-6}$	164 $\mu\text{m}$
Acrylate single coating	0.047	0.49	$100 \cdot 10^{-6}$	245 $\mu\text{m}$
Dual Acrylate inner coating	0.0042	0.44	$100 \cdot 10^{-6}$	190 $\mu\text{m}$
Dual Acrylate outer coating	0.85	0.44	$100 \cdot 10^{-6}$	245 $\mu\text{m}$
Carbon inner coating	45	0.3	$22 \cdot 10^{-6}$	30 nm

Table 2: Properties of fiber core/cladding and the different coating materials where  $E$  denotes Young's Modulus,  $\rho$  the poisson ratio and  $\alpha$  the CTE with  $r$  denoting the cladding diameter and fiber diameters with coating (including the cladding and inner coating where applicable) respectively. For Carbon the thickness of the inner coating layer is given.

fiber we need to consider the elasto-optic coefficients of the core material as a fiber under stress is an elasto-optic problem. As part of this thesis work four different coatings were analyzed: Aluminum, Single-Acrylate, Dual-Acrylate as well as a Copper-alloy and a bare fiber. The characterizing parameters for these four fibers are presented in table 2. As the laser source for testing has a wavelength of 606 nm while the operation wavelength for the design is 690 nm only fibers that have single mode operation at both wavelength were selected.

The **aluminum fiber** is a 1 m sample of the AIS4.3/125/175A fiber from fiberguide industries. The core, cladding and coating diameter are specified as  $(4.3 \pm 0.3) \mu\text{m}$ ,  $(125 \pm 3) \mu\text{m}$  and  $(175 \pm 18) \mu\text{m}$  respectively. As the uncertainty on coating diameter is unacceptable large, the coating thickness was measured under the microscope which yield  $(165 \pm 5) \mu\text{m}$ . Short and long term bending radius are further specified as 13 mm and 25 mm. The single-mode aluminum fiber has a working range specified as 633–680 nm. As the desired working wavelength is 690 nm and bending losses scale exponentially [29] the fiber was tested for bending losses at this wavelength with a wrapping radius of 3 cm and no significant losses were measured (see Appendix). The cut-off wavelength was specified by the manufacturer to be between 500 nm and 600 nm so that single-mode operation is still given for 606 nm. Mechanical parameters for aluminum are known and can be looked up in any handbook [30].

The **copper fiber** tested is a 3 m single-mode fiber by IVG fibers with the product number Cu600. The core, cladding and coating diameter were specified as  $(5 \pm 0.5) \mu\text{m}$ ,  $(125 \pm 1) \mu\text{m}$  and  $(164 \pm 5) \mu\text{m}$  with an operation wavelength of 600–800 nm. The coating material is not pure copper but a 99% copper alloy with small parts of nickel. Further the fiber has an inner coating consisting of a 10 – 30 nm of carbon. The cut-off wavelength is specified as lower than 560 nm. Mechanical parameters for copper and copper alloy are available in handbooks. [31] Parameters for Carbon were taken as specified in [32].

**Single and dual Acrylate** fibers are standard fibers supplied by Thorlabs and Newport respectively. They both have a core, cladding and coating diameter of  $(4 \pm 1) \mu\text{m}$ ,  $(125 \pm 1) \mu\text{m}$  and  $(245 \pm 15) \mu\text{m}$  respectively. Mechanical properties of the coatings are not commonly specified by the manufacturers and are not well-known although these coatings are very common. Especially information on Young’s Modulus is not widely available as in the case of Aluminum and Copper. The public available data found is given in table 3. The Analysis carried out by Olson is by far the most thorough incorporating several measurement techniques and repetitions with a good reproducibility [33]. The data presented in the most recent work by Michel et al. is on the same order of magnitude but does not specify separate values for the inner and outer coating of dual acrylate [34]. The data reported by Mitra et al. is off by orders of magnitude in the case of single acrylate and is further published on a company web page and not in a peer-reviewed journal [35]. I hence consider the data reported by Mitra et al. as an outlier and will from here on use the values reported by Olson et al.. Olson et al. further reports the inner coating of dual acrylate to have a thickness of 190  $\mu\text{m}$  in diameter.

Author	Single Acrylate/MPa	Dual Acrylate Inner Coating/MPa	Dual Acrylate Outer Coating /MPa
Olson, 2002 [33]	36.8-60.4	3.29-5.06	763 - 1043
Mitra et al., 2010 [35]	1500	1-1.7	650-950
Michel et al., 2015 [34]	6.7	-	2079

Table 3: Published Values of Young’s Modulus for Acrylate Coating

## 4.2 Thermal Stress

**Young's Modulus** An easy physical interpretation of Young's Modulus  $E$  is that it describes the stiffness of a material. A material with a high Young's Modulus or a high stiffness will be less likely to deform under stress, while a material with a low Young's Modulus will deform more easily when the same stress is applied. Mathematically Young's Modulus is given as the ratio of stress  $\sigma$  and strain  $\epsilon$  where the latter is given as the ratio of the length change  $\Delta L$  and the original length  $L$ :

$$E = \frac{\sigma}{\epsilon} \quad (16)$$

$$\epsilon = \frac{\Delta L}{L} \quad (17)$$

For a coated fiber Young's Modulus of the fiber coating is a measure of how well the deformation in the coating is passed on to the fiber core or put in other words how well the higher thermal expansion coefficient of the coating is translated to the fiber core as we will see later.

**Poisson ratio** The Poisson ratio  $\rho$  of a material describes the isotropicity of deformation processes in a material when stress is applied along an axial direction  $z$ . It is given as the ratio of the resulting transverse strain  $\epsilon_{trans}$  and axial strain  $\epsilon_z$

$$\rho = -\frac{d\epsilon_{trans}}{d\epsilon_z} \quad (18)$$

A Poisson ratio of 0.5 then describes a perfectly elastic material. In the case of thermal stress in a coated fiber we will see that a majority of the stress is along the longitudinal axis of the optical fiber. We will also see that radial and axial strain have opposite effects on the change of optical path with temperature. While being one of the four characterizing parameters, the Poisson ratio has however a subordinate effect as discussed in the following.

**Photoelastic effect for Thermal stress** As alluded to previously the photo-elastic effect in general describes how the optical characteristics of a medium change under the influence of mechanical stress or mechanical deformation. This effect is often made use of in fiber sensors being a major industrial application of specialized optical fibers. A obvious example is the use of fiber Bragg gratings as strain sensors but more sophisticated fiber sensors based on the photoelastic effect to detect voltage and pressure have likewise been developed [9]. For an optical fiber the photoelastic effect due to thermal stress has been derived to yield the following:[36]

$$\frac{1}{L} \frac{d(nL)}{dT} = n\epsilon_z + \frac{\partial n}{\partial T} - \frac{1}{2}n^3 [P_{12}\epsilon_z + (P_{11} + P_{12})\epsilon_r] \quad (19)$$

$$= 9.1 \cdot 10^{-6} + 1.04\epsilon_z - 0.61\epsilon_r \quad (20)$$

where  $\epsilon_z$  and  $\epsilon_r$  denote the axial and radial strain respectively and  $P_{11}$  and  $P_{12}$  represent the photo-elastic coefficients of silica glass. It should be noted for the careful reader that this is analogous to the Pockels effect given as  $n(E) \approx n - \frac{1}{2}rn^3E$  with  $r$  being the Pockels coefficient [16]. Arbitrary strains and their effect on an optical material can be analyzed using the Strain-Optic Matrix (see e.g. Saleh *et al.* [16]).

### 4.3 Analytic Solution

While the thermal characteristics of the fiber have been described above as given in equation 20, it remains to quantify the axial and radial strain. An analytic solution for the thermal stress in coated fibers was first derived by Lagakos *et al.* [36] and has been refined for metal-coated fibers by Shieue *et al.* [37]. The equations given in those papers are directly used with the parameters for the different coating materials to derive an analytic description of their thermal characteristics and are given in the Appendix, section 8. An overview of the results is given in the table below. Uncertainties arise from uncertainties on the coating thickness specified by the manufacturer.

Fiber	Analytic Result $\frac{1}{L} \frac{d(nL)}{dT}$
Single Acrylate	$(9.32 \pm 0.2) \cdot 10^{-6} \text{ K}^{-1}$
Aluminum	$(18.4 \pm 0.7) \cdot 10^{-6} \text{ K}^{-1}$
Copper	$(17.3 \pm 0.5) \cdot 10^{-6} \text{ K}^{-1}$
Bare	$9.6 \cdot 10^{-6} \text{ K}^{-1}$

Table 4: Analytic Results for Thermal Sensitivity of Different Coated Fibers

The Copper fiber was modelled neglecting the carbon layer and assuming poor copper as 99% copper does not exhibit significantly different properties than pure copper [31]. Further a result for dual acrylate was not derived as additional layers increase the complexity of the model and surpass what was presented by Shieue *et al.* [37].

As the aluminum fiber is as expected the most promising candidate for a fiber with an increased temperature sensitivity further analysis is carried out looking at the parameters describing this fiber. The thermal sensitivity of the optical path length  $1/L d(nL)/dT$  is plotted along with the axial and radial strain as function of cladding and coating diameter as well as Young's Modulus and the Poisson ratio. The thermo-optic coefficient is also indicated as a reference as it adds up to the thermal sensitivity along with axial and radial strain where axial and radial strain have opposing effects. The result of this analysis is presented in figure 11.

As we can see axial and radial strain as well as the overall thermal sensitivity all follow similar trends throughout the calculations. These quantities are increasing with increasing coating diameter, Young's Modulus and Poisson ratio while they are decreasing with cladding diameter. These results do agree with expectations as with an increasing coating diameter the higher thermal expansion coefficient of the coating will dominate. The thermal sensitivity for increasing coating diameter reaches a plateau roughly corresponding to the sum of thermal expansion coefficient of the coating and thermo-optic coefficient of the core. Likewise, as Young's Modulus describes the stiffness of the coating material, induced strain will increase with increasing stiffness. A much softer coating material lets the coating expand without having a major impact on a much stiffer core and cladding material as it is much more resistant to deformation. Aluminum and silica glass have a well-matched elastic modulus.

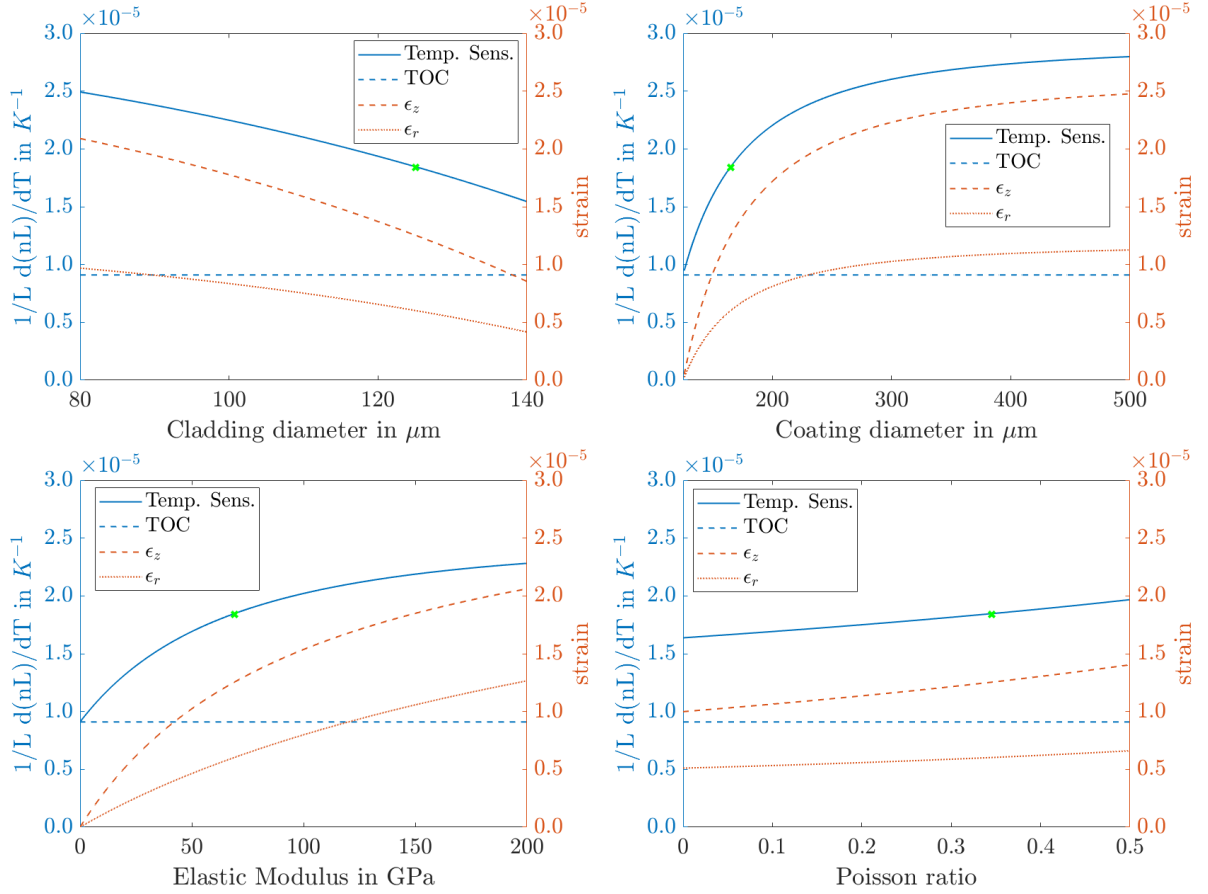


Figure 11: Thermal Characteristics of the Optical Fiber as function of the different model input parameters. The overall temperature sensitivity of the optical path length is plotted along with the axial strain  $\epsilon_z$ , radial strain  $\epsilon_r$  and thermo-optic coefficient TOC. The temperature sensitivity of the aluminum-coated fiber used (ASI4.3/125/175A) is marked as a reference in green and its parameters are used as the default. Top left: Dependency on the cladding diameter with all other parameters chosen to describe the aluminum-coated fiber (ASI4.3/125/175A). Top right: Dependency on coating diameter. Bottom left: Dependency on the Young's Modulus. Bottom right: Dependency on the Poisson ratio.

A decrease in cladding diameter while the coating diameter stays constant, increases the ratio of coating material and silica glass leading to a similar effect as an increase in coating diameter.

Coating diameter and Young's modulus play a dominating role in determining the behaviour of the fiber followed by the cladding diameter and lastly the Poisson ratio with a secondary role. One reason for the subordinate effect of the Poisson ratio of the coating material lies in the geometry of the fiber as it is much longer than it is wide the geometry already largely determines axial and radial strain.

Provided that analytic results will be in good agreement with experimental results it is now further interesting to think about a custom-designed fiber and the increase and temperature sensitivity such a fiber could have. We thus tweak the parameters as given in table 5 using an aluminum coating which yields a thermal sensitivity of  $28 \cdot 10^{-6} K^{-1}$  which is three times that of a single acrylate fiber. The cladding diameter is chosen as

Parameter	Value
Coating Material	Aluminum
Cladding diameter	80 $\mu\text{m}$
Coating diameter	250 $\mu\text{m}$
Thermal Sensitivity	$28 \cdot 10^{-6} \text{ K}^{-1}$

Table 5: Parameters for a custom-made fiber with increased thermal sensitivity

80  $\mu\text{m}$  as custom made fibers with such a reduced cladding are commercially available with variable coating thicknesses and materials [38]. Having a thicker coating also has the added benefit that the temperature sensitivity changes less with small variations in the coating thickness.

#### 4.4 Simulation

The analytic results presented in the previous section were compared with a finite element method simulation carried out with COMSOL. In addition, the simulation gave the possibility to model fibers with more than one coating in an easier way. Analysis on radial and axial strain was split up into two different simulations. Since the problem of thermal stress is satisfactorily solved with a classic approach, COMSOL is a suitable choice modelling all key parameters.

COMSOL provides a module simulating thermal stress that was applied to this problem. It further allows to solve for principal strain and stress components and temperature. To carry out these simulations the same parameters were used as in the case of the analytic calculations with the exception of the copper fiber where a 30 nm layer of copper was added as specified by the manufacturer but had no noticeable effect on the simulation results.

To analyze the radial strain we considered an infinitesimal small piece of fiber implemented in form of a 2D simulation of the crosssectional area of the fiber. The validity of the model was tested by comparing with a 3D model with fixed boundary conditions as well as a 3D radial symmetric model with only one fixed boundary. All three models deliver the same result while the first model is the mathematical correct approximation and requires the least computation time. An example of the results of a COMSOL simulation for radial strain is presented in figure 12. In order to analyze the axial strain a 3D model based on radial symmetry was established. Modelling the axial strain in COMSOL was a particular challenge due to the very different dimensions of thickness and length of an optical fiber.

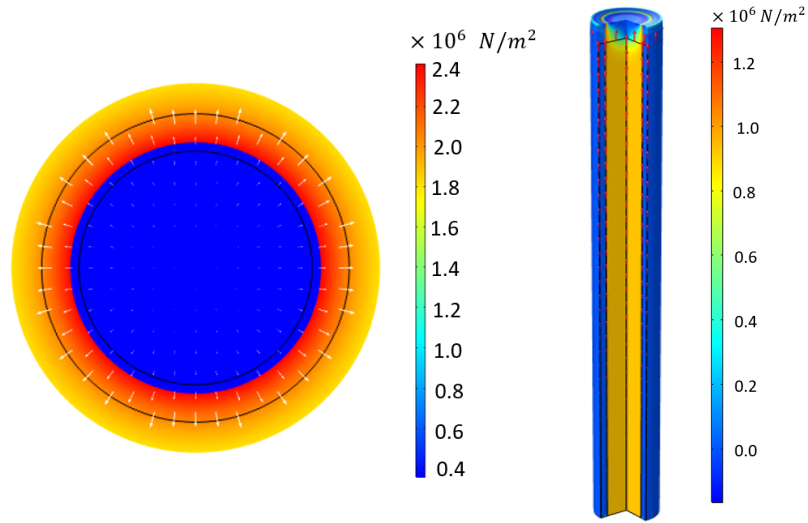


Figure 12: Exemplary COMSOL Simulation for radial and axial stress using the parameters of the aluminum coated fiber

This problem was solved by starting off by modelling a short piece of optical fiber in the radial symmetric model with one fixed end and increasing the length only until the value for the axial strain stays constant as it approaches its real value asymptotically. The simulated values for radial and axial strain for each fiber then yield the following thermal sensitivities for the different fibers:

Fiber	Simulation Result $\frac{1}{L} \frac{d(nL)}{dT}$	Analytic Result $\frac{1}{L} \frac{d(nL)}{dT}$
Single Acrylate	$(9.34 \pm 0.2) \cdot 10^{-6} \text{ K}^{-1}$	$(9.32 \pm 0.2) \cdot 10^{-6} \text{ K}^{-1}$
Aluminum	$(17.7 \pm 0.7) \cdot 10^{-6} \text{ K}^{-1}$	$(18.4 \pm 0.7) \cdot 10^{-6} \text{ K}^{-1}$
Copper	$(16.5 \pm 0.5) \cdot 10^{-6} \text{ K}^{-1}$	$(17.3 \pm 0.5) \cdot 10^{-6} \text{ K}^{-1}$
Dual Acrylate	$(10.5 \pm 0.4) \cdot 10^{-6} \text{ K}^{-1}$	-
Custom fiber	$(26) \cdot 10^{-6} \text{ K}^{-1}$	$(28) \cdot 10^{-6} \text{ K}^{-1}$

Table 6: Comsol results for thermal sensitivity of different coated fibers in comparison with the analytically derived result

It should be noted that no significant difference was noticed when modelling the copper fiber with or without the carbon layer. Choosing a mesh that would have small enough elements for the carbon layer but not lead to a too large computational time was extremely difficult and it can not be excluded that deviations arise as a result. We further list the result for the custom made fiber to increase thermal sensitivity suggested in the previous section. Analytic results are given for comparison. In general, the simulated results are a bit lower than the analytic results. A reason for this could not be identified.

## 5 Experimental Study

High precision measurements of the thermal sensitivity of coated fibers are not trivial to carry out. In general all measurement techniques are based on phase measurements i.e. fringe counting where the fringes are a result of destructive and constructive interference arising as the optical path length changes. In the past, MZIs placed in a liquid thermal bath have been used and changes in the interference pattern were observed and evaluated. This method has multiple downsides. For instance it takes some effort to gain good and stable fringe visibility in the form of vibration isolation or other measures [39]. Further, problems with measurements around room temperature were cited due to increased thermal fluctuations [39]. An alternative approach to measuring the thermal sensitivity of optical fibers is to use them as a Fabry-Pérot interferometer (FPI). In one form this was established by Li et al. using a broadband light source [40]. This light was coupled into a MI with a few mm FPI out of tellurite and germanate respectively spliced on to one of the ends and a wavelength meter at the output to record the spectrum and interference and thus deriving phase information [40]. Main drawbacks are that due to the short length only few fringes will be observed and achievement of a uniform temperature distribution of the FPI of interest is difficult to achieve without impacting the fiber it is spliced to.

Here, the idea of using the fiber as a FPI is established vastly differently and in this configuration measurements to determine the thermal sensitivity of optical fibers are carried out for the first time to my knowledge.

This section is organized in three parts. In the first part I will outline the principles and theory, in the second part I will explain the set up and its design and lastly I will explain experimental methods and procedure. Introduction to the data analysis method as well as results of the experiments can be found in the next section.

### 5.1 Principle

While commonly FPI devices are used as frequency filters or for calibration when a laser is scanned in frequency one can just as well keep the frequency stable and scan the optical path length instead by ramping the temperature.

A FPI consists of two surfaces, in the simplest case two mirrors, with reflectance  $R_1$  and  $R_2$ . The finesse  $\mathcal{F}$  describing effectively how sharp the frequency discrimination of a FPI is, is then given by

$$\mathcal{F} \approx \frac{\pi \sqrt[4]{|R_1 R_2|}}{1 - \sqrt{|R_1 R_2|}} \quad (21)$$

The transmittance  $T$  is then given as

$$T(\nu) = \tau_{max} / \left( 1 + \left( \frac{2\mathcal{F}}{\pi} \right)^2 \sin^2 \left( \frac{\pi\nu}{\nu_F} \right) \right)^2 \quad (22)$$

where  $\tau_{max}$  denotes the maximum transmittance,  $\nu$  the frequency and  $\nu_F$  the free spectral range given as  $c/2nL$ . A detailed derivation of this can be found in Fundamentals of

Photonics [16]. Using the expression for the free spectral range this can easily be rewritten as a function of optical path in the following way:

$$T(nL) = \tau_{max} / \left( 1 + \left( \frac{2\mathcal{F}}{\pi} \right)^2 \sin^2 \left( \frac{\pi\nu 2nL}{c} \right) \right) \quad (23)$$

The reflectivity  $R$  is given as  $1 - T$ . Rewriting as function of optical path length of course assumes a light source with a constant frequency, an assumption that will only hold up for very narrow linewidth lasers. The free spectral range for a 1 m long fiber cavity can be calculated to roughly be 100 MHz, the linewidth of the laser should be several orders of magnitude below that. For these experiments a dye laser with a 10 Hz linewidth was available with an operating wavelength of 606 nm.

A simple approach to model the reflectivity of a fiber cavity can now be developed based on these equations. Firstly, we derive the reflectivity of an fiber end using Fresnel equations where  $n_1 = 1.44$  is the refractive index of a fiber core and  $n_2 = 1$  is the refractive index of air. For a laser beam incident with 90 degrees on a transition of two materials this yields

$$R_1 = R_2 = \left( \frac{n_1 - n_2}{n_1 + n_2} \right)^2 = 0.032 \quad (24)$$

which results in a finesse of 0.58. For a small finesse as the case for this fiber cavity a Taylor approximation of the form  $\frac{1}{1+x} \approx 1 - x$  can be made for equation 23. Further using the trigonometric identity  $\sin^2(\Theta) = \frac{1 - \cos(2\Theta)}{2}$  and setting  $\tau_{max}$  to 1 this yields:

$$T(\nu) \approx \left( 1 - 2 \left( \frac{\mathcal{F}}{\pi} \right)^2 + 2 \left( \frac{\mathcal{F}}{\pi} \right)^2 \cos \left( \frac{4\pi\nu nL}{c} \right) \right) \quad (25)$$

$$R(\nu) \approx 2 \left( \frac{\mathcal{F}}{\pi} \right)^2 - 2 \left( \frac{\mathcal{F}}{\pi} \right)^2 \cos \left( \underbrace{\frac{4\pi\nu nL}{c}}_{\varphi} \right) \quad (26)$$

A detailed derivation can be found in the Appendix, section 8. The relation between the phase  $\varphi$  and the optical path  $nL$  as well as their temperature derivatives now becomes obvious and is given as:

$$\varphi = \frac{4\pi nL}{\lambda} \longrightarrow \frac{d\varphi}{dT} = \frac{4\pi}{\lambda} \frac{d(nL)}{dT} \quad (27)$$

Note that a factor of  $4\pi$  is obtained while naively a factor of  $2\pi$  might be expected as the case for a fiber interferometer. For a more intuitive approach to understand this better, we consider that in data analysis every fringe will be given as a phase difference of  $2\pi$  corresponding to a change of the optical path length of  $\lambda/2$ . From this considerations we then obtain

$$\frac{d\varphi}{2\pi} = \frac{d(nL)}{\lambda/2} \longrightarrow \frac{d\varphi}{dT} = \frac{4\pi}{\lambda} \frac{d(nL)}{dT} \quad (28)$$

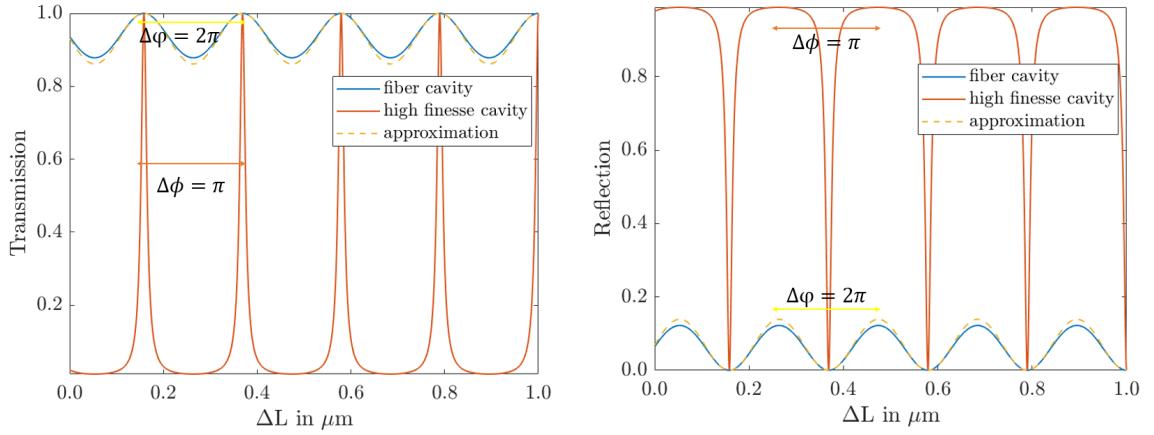


Figure 13: Left: Transmission of a fiber cavity in comparison with a high finesse cavity ( $F=14.88$ ). Low finesse broadens the peaks and leads to a lower variation in transmission. The phase difference between two maxima according to the standing wave condition is  $\pi$  while when modelling the transmission of the fiber cavity as a cosine this corresponds to a phase difference of  $2\pi$  in the model. Right: Reflectivity of a fiber cavity compared with a high finesse cavity in analogy to the transmission.

Comparing the transmission and reflection for a fiber cavity with a high finesse cavity as depicted in figure 13 we see that the resonance peaks are much broadened due to the low Finesse ( $F = 0.58$ ) of the optical fiber. According to the standing wave condition  $m\frac{\lambda}{2} = nL$  and equation 23 maxima are separated by a phase shift of  $\Delta\phi = \pi$  which is not to be confused with the phase  $\varphi$  discussed above that is the relevant quantity for data analysis (see section 6.1).

The difference between maximum and minimum transmission is 0.12 giving the modulation depth.

There are several advantages in studying the reflection instead of transmission. For one, theoretically this method should be less sensitive to intensity fluctuations of the laser as at least in theory we expect the signal to go down to 0 intensity. In the same varying coupling efficiency or other noise caused by vibrations should impact the signal to noise ratio less. Other advantages lie in the experimental set up which we will discuss in section 5.2.

## 5.2 Experimental Set Up

After the illustration of the experimental principle, we will now discuss the practical implementation of the experiment.

### 5.2.1 Design of a Heat box

A crucial part of the experimental set up is a way to ramp the temperature of the optical fiber in a controlled manner. Several options were considered here. A common way to solve this problem is a thermal bath. While homogeneous heating can easily be achieved with constant mixing, a thermal bath is hazardous as electronics is involved and spilling can easily result in an accident. Further, perturbations introduced by mixing or otherwise

caused movement of the liquid can reduce the signal to noise ratio. Lastly, the fiber ends can not be in water as this changes the reflectivity to 0.15%. Since as much fiber as possible should be heated this is not ideal. Instead, a decision was made to build a heat box.

A key criteria is that it should be possible to control the heating rate with a computer. Thus, the heat element is chosen to be an aluminum plate with HS15 1R0 J resistors as depicted in figure 14 that are connected to a voltage source (Voltcraft PPS13610) which is controlled with a LabView program written particularly for this purpose. The power per resistor is given by the manufacturer as 15 Watts with a resistance of  $1\ \Omega$ . The power supply used is the PPS 13610 with a maximum output voltage of 18 V and a maximum output current of 20 A. To have a suitable power at all heat resistors, the equivalent resistance of the circuit should hence roughly be  $R_{eq} = \frac{U}{I} = 0.9\ \Omega$ . It optimizes the power at every resistor and thus the heat generated, while still allowing slow temperature ramping. As we will not want to run at maximum power and voltage the circuit was chosen to consist of 12 resistors. Four at a time are soldered in a row and then connected in a parallel circuit yielding an over all resistance of:

$$R_{eq} = \frac{1}{R_1 + R_2 + R_3 + R_4} + \frac{1}{R_5 + R_6 + R_7 + R_8} + \frac{1}{R_9 + R_{10} + R_{11} + R_{12}} = 0.75\ \Omega \quad (29)$$

The aluminum plate has dimensions of  $(20 \times 23 \times 0.3)\ \text{cm}^3$ . The single resistors are clamped on the Aluminum plate with thermal paste between the resistors and the plate to improve thermal conductivity. All resistors were connected with cable with a diameter of 2 mm to minimize additional resistance. The spacing between the resistors was chosen equally across the plate to ensure homogeneous heating as best as possible.

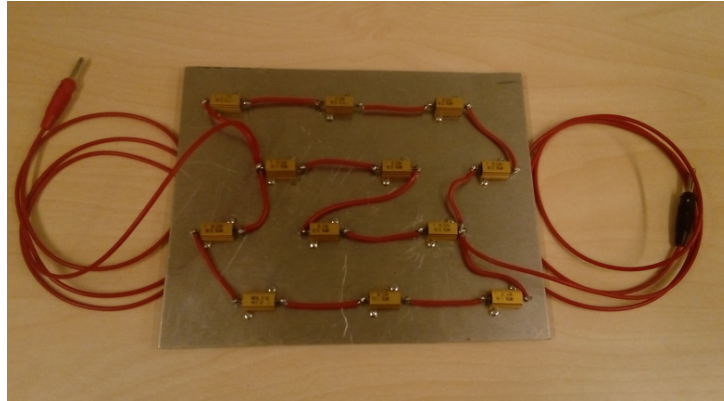


Figure 14: Aluminum heat plate with 12 resistors with a  $1\ \Omega$  resistance each and a power of 15 Watts.

The insulation material used is armafex with a thermal conductivity of  $0.031\ \frac{\text{W}}{\text{m}\cdot\text{K}}$  and a thickness of approximately 1 cm. One layer of armafex was placed on the bottom of a cardboard box with the dimensions  $(20 \times 25 \times 15)\ \text{cm}^3$ . On top of the armafex the heat source was placed with the resistors facing the bottom so that we have a flat, homogeneous surface upon which we can place the fiber spool. On top of the fiber spool we place an additional layer of armafex. All sides of the cardboard have one layer of insulation on the outside. With exception of the top layer they are glued on using contact adhesive to reduce air enclosures and other inhomogeneities.

A temperature sensor is placed in the middle of the downside of the fiber spool facing the aluminum plate using electrical tape. Long term measurements over five and a half hours comparing the achieved temperature stability with the temperature stability of the lab environment outside of the box found a variance of  $0.009^{\circ}\text{C}$  and  $0.04^{\circ}\text{C}$  respectively showing an improvement of a factor of 4.3. This further shows that an assumed long-term stability of  $0.01\text{ K}$  (see section 3) is realistic with simple thermal insulation in form of a box with thermal insulation material.

**Characterisation of the Heating Process** Before introducing optical fibers to the set up, the heating properties of the aluminum plate were characterized. For initial testing of the experiment it was initially thought to be important to increase temperature linearly with time to exclude any deviations or irregularities originating from the heating process. Equally, slow ramping was desirable to make sure the fiber can be approximated to be in thermal equilibrium with the environment during heating. Noise originally observed due to convection could be minimized by placing the aluminum plate between two layers of armaflex as described above. The desired heating characteristics could be achieved by setting the voltage to  $1.3\text{ V}$  and increasing it by  $0.1\text{ V}$  every ten minutes. The resulting heating process is depicted in figure 15 (left).

During the course of the experiments it was found that it is desirable to observe fringes at a higher frequency and thus faster heating was necessary. After initial experiments with the slow linear heating process it was further found that smaller nonlinearities do not present a problem in the data analysis so that a second setting for faster ramping was chosen with a constant voltage of  $5\text{ V}$ , see figure 15 (right).

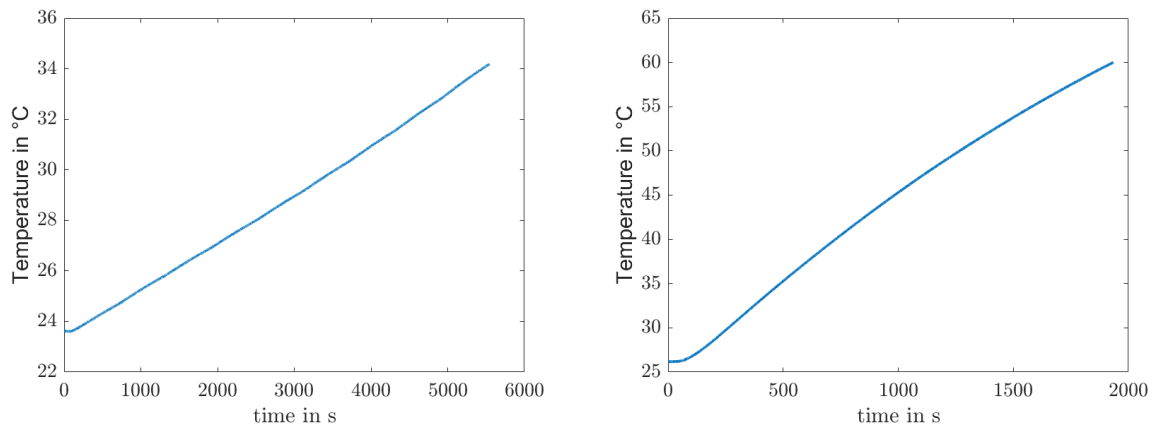


Figure 15: left: slow, linear ramping of temperature using an aluminum plate with 12 resistors as a heat plate. The voltage is set to  $1.3\text{ V}$  and increased by  $0.1\text{ V}$  every ten minutes, right: Heating of an aluminum plate with 12 resistors at a constant voltage setting of  $5\text{ V}$

### 5.2.2 Optical Set Up

As mentioned previously, in order to observe fringes from a fiber cavity a laser source with a considerably narrower linewidth than the cavity linewidth is required. The dye laser used is stabilized to an ultra-low expansion cavity placed in a vacuum chamber. The ULE cavity is further placed on an active vibration isolation platform. A locking mechanism locks to the  $TEM_{00}$  mode and gives feedback to an EOM placed in the ring cavity of

the laser. The set up and locking scheme is rather complex and a detailed explanation can be found in the PhD thesis "Light-Matter Interaction and Quantum Computing in Rare-Earth-Ion-Doped Crystals" by Adam Kinos[41]. The linewidth achieved is 10 Hz which is a factor of  $10^7$  smaller than the free spectral range of a 1 m fiber cavity. Any errors from the linewidth can thus be neglected when the laser is locked.

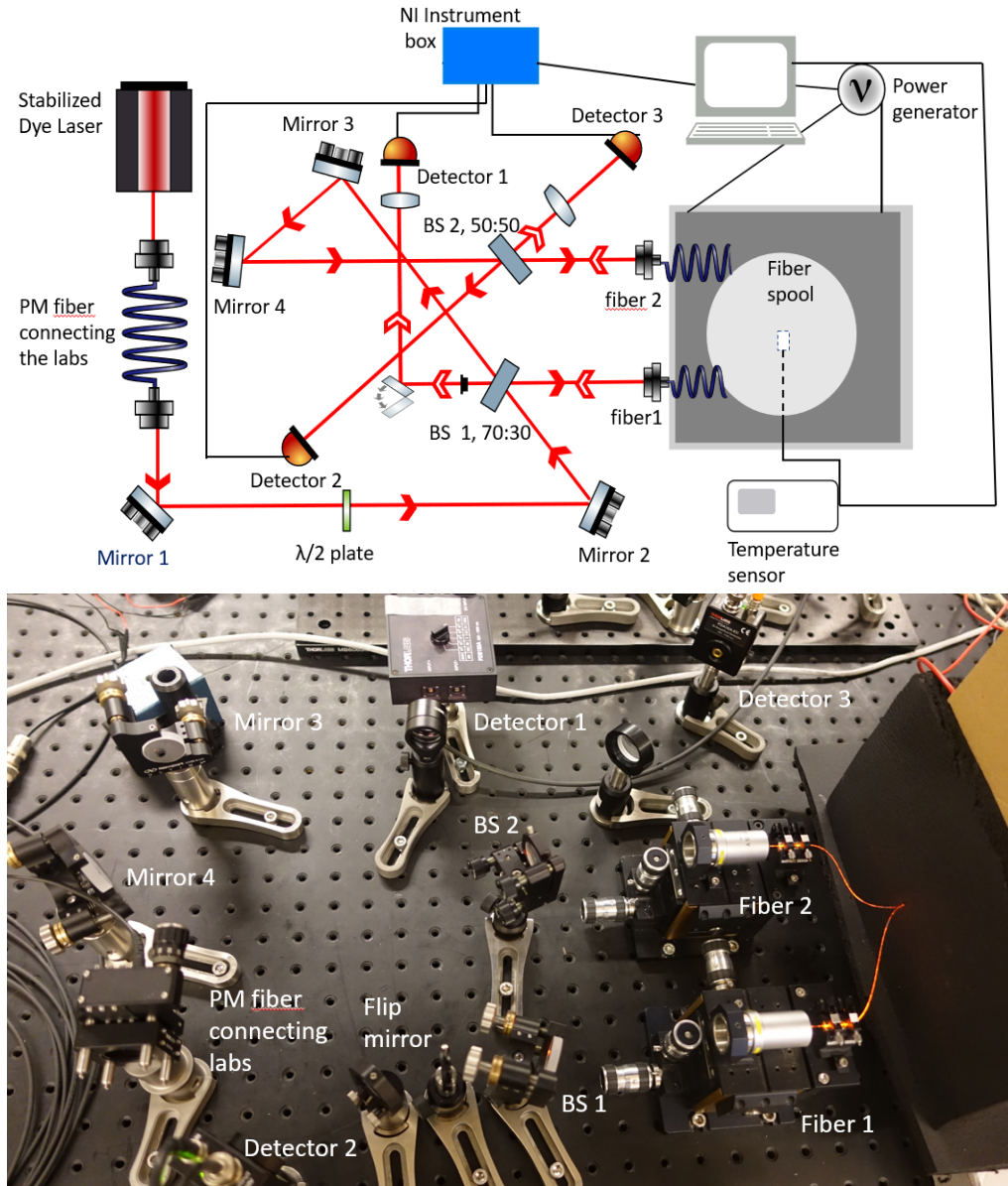


Figure 16: Optical set up to measure the thermal sensitivity of optical fibers with different coatings. The reflection of the fiber cavities is measured and their intensity recorded as a function of time as well as the intensity of a reference beam. The fiber is coiled and placed on an aluminum heat plate with a temperature sensor in the middle recording temperature as a function of time allowing interpolation to gain temperature-dependent phase information. Red errors indicate propagation of laser light before being coupled into fiber 1 or 2, white errors indicate light reflected from the fibers propagating back.

Not locked to the ULE cavity the laser linewidth is about 1 MHz. In addition to that,

the laser may drift uncontrolled. The fringes due to a change in frequency would then be overlapping with fringes due to optical path change and thus data can only be taken and evaluated with the laser locked at all times. The laser further has an option to be scanned mode-hop free up to 20 GHz, although then not locked to the ULE cavity.

The dye laser is placed in a lab separately from the set up which is placed on an optical table in a different lab. Both are connected with an polarization-maintaining fiber by Kirchhoff and Schäffner (PMC-630-3,8-NA012-3-APC-2500-P) that was established as a connection between both labs as part of this work. About 1% of the stabilized laser output power is sent through this fiber. The power finally available on the experimental table with my set up varied between 1 – 2 mW. The output of the fiber is aligned to be vertically polarized. The optical set up is illustrated in figure 16.

The out-coupled laser beam is directed by two mirrors, mirror 1 and mirror 2, before hitting beam splitter 1 with a splitting ratio of 70:30. 30% of the incident light is reflected and coupled into optical fiber 1 placed on a fiber stage with a 10 mm objective. As the fibers were not perfectly mode matched the achieved coupling efficiency was about 30% so that around 100  $\mu$ W of output power could be achieved. The reflection of the fiber cavity is detected after transmission through beam splitter 1 with a Thorlabs balanced photodetector PDB 150-A, detector 1 in figure 16. The reflection is separated from backreflections of the rest of the set up with a pinhole. A flip mirror makes alignment of the detector easier. With a calculated reflected intensity of 12% we thus expect about 12  $\mu$ W. This is indeed in good agreement with measurements throughout the course of experiments.

The 70% transmitted light after the beam splitter are directed by another two mirrors, mirrors 3 and 4, which are used to align coupling into the fiber 2. Following those two mirrors the beam is incident on beam splitter 2 with a ratio of 50:50. The reflected beam is used as a reference beam and aligned with an amplified photodetector, detector 2, with the product number PDA 36A-EC by Thorlabs. The transmitted beam is coupled into optical fiber 2 placed on an identical fiber stage with an identical objective. The ratios of the beamsplitters are chosen in such a way that a similar output power of 100  $\mu$ W can be achieved on this fiber as well. The reflection of the fiber cavity of roughly 16  $\mu$ W is picked up as reflection of beam splitter 2 when propagating back. The photodetector is the same model as the reference detector. All photodetectors used have switchable gain that was set to around 6 dB in the case of the photodetectors detecting fringes and around 20 dB for the reference detector. The gain was adjusted throughout the course of experiments as needed. Communication between the detectors and the computer was facilitated with the NI instrument box USB-6211.

Both optical fibers are wrapped on the same spool with the path of the two fibers being as similar as possible.

Upon completion of the experimental set-up, experiments were carried out as described in the following.

### 5.3 Experimental Procedure

Fiber preparation was more complicated in case of the metal-coated fibers and the bare fiber and details are given in the Appendix, section 8. All fibers were first stripped of their coating on the ends and then cleaved to ensure good mode-coupling.

Initial testing of the set up and use of the fibers as fiber cavity was performed by

scanning the available laser source mode-hop free over a range of 20 GHz with a single acrylate fiber with a fiber length of 4.65 m. Clearly visible fringes could be observed. An exemplary plot can be found in the Appendix, section 8. The length of the fiber is directly proportional to the free spectral range determining the frequency at which fringes appear. Keeping the set up initially as simple as possible was further deemed reasonable and means a maximum intensity available for detection of fringes and thus provides a better contrast.

The length of the optical fiber is a crucial parameter to obtain the optical path change with temperature normalized with length. The length of the fiber was measured after completing measurements on it as recleaving was often necessary. For this, the fiber is marked with optical tape where it is launched into the heat box and then measured with a folding ruler. That the fiber piece outside the box does not heat up, and can therefore be neglected, was confirmed in a time-dependent COMSOL simulation (see Appendix, section 8).

In a next step two acrylate fibers of similar length were measured to provide a reference how well temperature characterization of the fibers with the given set up can be expected to work. Deviations for the two fibers in these measurements should be considered as an experimental limit. The lengths of the fibers are chosen to be about 1 m as this corresponds to the length of the aluminum fiber sample provided and looking at the analytic results and results of the simulation this is the fiber we are most interested in.

I proceeded to measure the 1 m aluminum, 3 m copper and 10 m dual acrylate fiber with a single acrylate fiber as reference fiber. The length of the reference fiber was matched to the length of the experimental fiber with the exception of dual acrylate as only a maximum length of 5 m reference fiber was available. Measuring with a reference is deemed crucial as fluctuations of the experimental environment will be the same for both fibers and we expect to have better control of the ratio than the absolute value of the thermal sensitivity. Before and after every measurement the intensity background without light is recorded. Further, long-term measurements were carried out to test variations of the intensity background with time and it was found that the background and its variation is constant with time.

**Comparison of Cooling and Heating** Throughout the course of the experiments cooling was recorded when possible. Due to the long time duration issues occurred due to other experiments operating with the same laser and the laser jumping out of lock. In addition data obtained from cooling was often very noisy and could thus not be analyzed in a sensible manner. Nevertheless it is essential to carry out analysis regarding whether similar results are obtained for the heating and cooling process. As only enough data sets were available for the single acrylate fiber, only results for this fiber in this regard will be presented.

**Experimental Challenges** A first issue was that throughout the course of these experiments, the locking did not always work reliably. Perturbations such as vibrations and acoustic noise can lead to the laser jumping out of lock. During periods of experiments the laser could only be kept locked for about an hour. Main reason for this is most likely old dye and dye leaking. The unreliability of the locking limited experimental possibilities to relatively short experiments during that time. Once the dye was refilled laser locking

worked very reliable.

A second practical problem throughout the course of experiments was the launch of the fiber into the heat box. This required drilling a hole into the box. In the beginning of the experiments this was not of an issue as the hole was very small and armaflex has the property to resume its shape after brief deformation so that the armaflex layer enclosed the optical fiber tightly. However, throughout the course of the experiments it became necessary to put a small straw through the hole to be able to guide a fiber without breaking the end. This was in particular an issue for the bare fiber so that widening of the hole and thus an decrease in thermal insulation was unavoidable.

Another point that was an interesting observation to make was the effect of polarization on the measurement data. As pointed out previously when discussing polarization controllers, bending and coiling a fiber induces birefringence in a fiber. We observed that for some coated fibers a beating from the two different polarization axis was obtained. This is due to different polarizations experiencing a slight difference in refractive index thus seeing a slightly deviated cavity length. As we can see this difference is very small as the beating is only about three fringes compared with thousands of fringes recorded overall. This can become a problem when sitting at the node of this beating when trying to detect fringes. However, an easy solution was found by inserting a  $\lambda/2$  plate in the set up and readjusting it. It is interesting to note that the beating was particularly strong for the aluminum fiber which could indicate that it has more birefringence, at least when coiled.

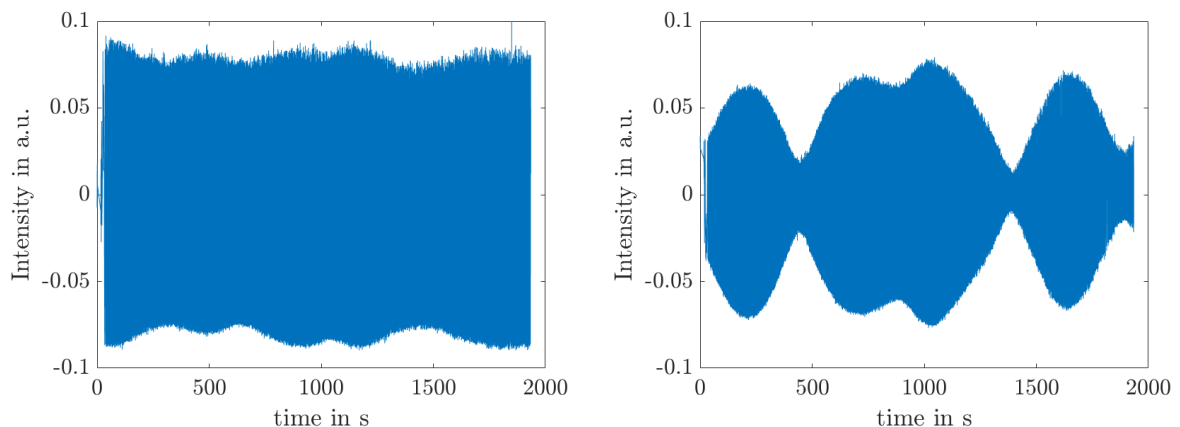


Figure 17: Left: Normal recording of fringes with no beating Right: Recording of fringes with an observed beating of the different polarizations for the aluminum fiber before inserting a  $\lambda/2$  plate into the set up.

The most difficult experimental challenge to overcome presented itself in the permanent disappearance of any fringes. Finally, the reason was found to be a combination of the cleaver working unreliably, an issue that will need to be addressed for future experiments, and polarization that was resolved by introducing a  $\lambda/2$ -plate to the set-up.

## 6 Results

Before presenting the results of the experiments I described above, a short explanation of the data processing is given.

### 6.1 Data Analysis

In a first step we subtract the intensity background from both the data recorded by the detectors monitoring the intensity of the back reflection of the fibers and divide by the intensity recorded by the reference detector to correct for any fluctuations intrinsic to the laser.

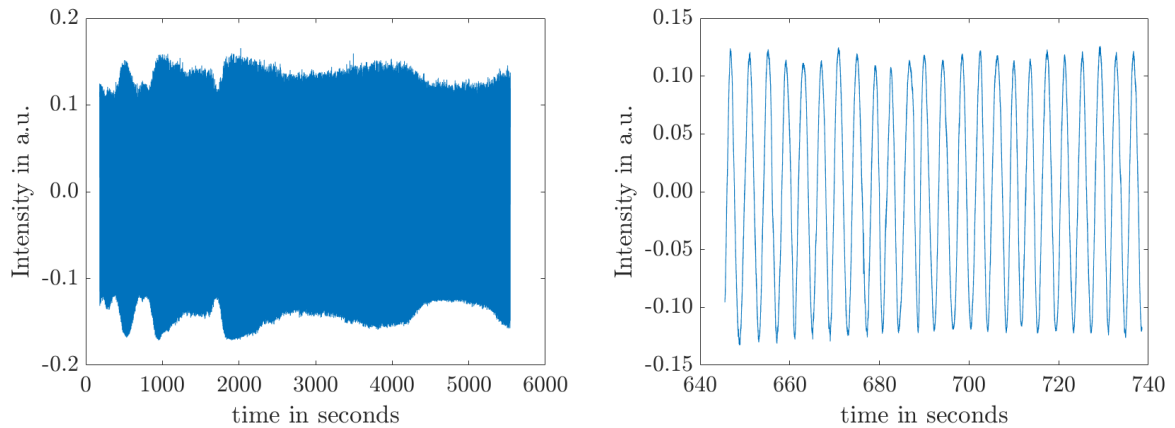


Figure 18: Example of recorded data as a result of temperature ramping. Each fringe presents a  $\pi$  phase shift and thus a change in optical length of the fiber equal to  $\frac{\lambda}{2}$ . left: Complete set of data recorded over a course of two and half hours while the temperature is ramped linearly according to figure 15 left. The laser is locked and has a design linewidth of 10 Hz right: 100 sec of measurement

While we record intensity  $I$  as a function of time  $t$  as presented in figure 18 and temperature  $T$  as a function of time the quantity we are truly interested in is the phase  $\varphi$  of the signal as a function of temperature since we have seen previously that this is directly proportional to the optical path change ( $\frac{d(nL)}{dT}$ ) with temperature:

$$\frac{d\varphi}{dT} = \frac{4\pi}{\lambda} \cdot \frac{d(nL)}{dT} \quad (30)$$

The phase is extracted by using Fourier transforms to convert real data into complex data. A detailed explanation is given in the Appendix, section 8. An exemplary comparison is of original and transformed data is presented in figure 19.

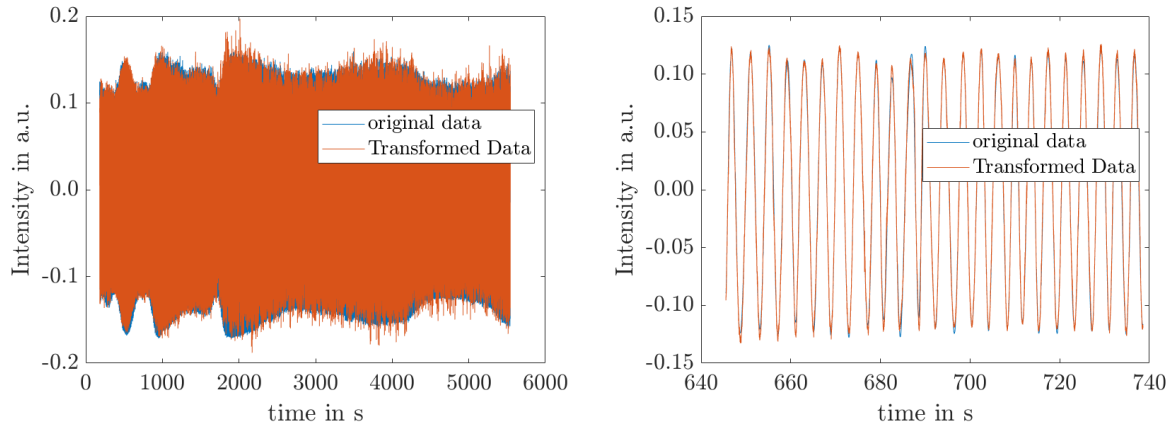


Figure 19: Comparison of experimental data with transformed and filtered data. The data processing consists of the following steps: 1) Fourier transform of the data. 2) Filtering with a Supergaussian 3) Inverse Fourier Transform. The real part of the processed data is plotted as amplitude of the intensity signal.

The phase is obtained by use of the angle function build-in to MATLAB that gives the unwrapped phase angle for each data point. This now results in phase as a function of time (see figure 20 left). Finally, interpolation is used to gain optical path as function of temperature as temperature and intensity are sampled at different rates, see figure 20 right.

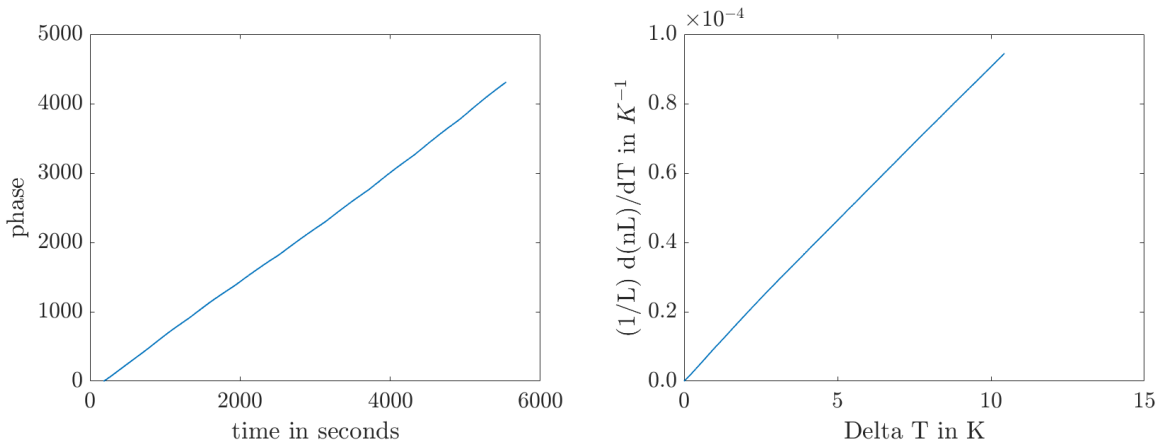


Figure 20: Left: Derived Phase change as a function of time. The phase of each data point is derived by using Fourier transforms to convert the measurement data into complex data. Right: Optical Path Length Change with Temperature obtained by using the spline interpolation to resample the time-dependent data as temperature-dependent and the relation  $1/Ld(nL)/dT = \frac{\lambda}{4\pi L} \phi$

## 6.2 Thermal Sensitivity of Coated Fibers

The resulting thermal sensitivity of the optical path length for a single acrylate fiber with a length of 4.65 m was measured as  $9.013 \cdot 10^{-6} \text{ K}^{-1}$  during a heating process with slow linear heating and as  $9.952 \cdot 10^{-6} \text{ K}^{-1}$  during a cooling process.

Measurements with two fibers were additionally carried out with a linear slow heating

rate. As the fibers were much shorter, this resulted in fringes at a much lower frequency where a lot of noise was observed and filtering was difficult. A faster heating process was thus used making analysis easier and yielding an improved signal to noise ratio. The result of measurements with two single acrylate fibers in parallel are presented in figure 21. Minimal deviations are observed while overall measurements of both fibers agree extremely well. The linear fit to the pictured results yields a thermal sensitivity of  $8.952 \cdot 10^{-6} \text{ K}^{-1}$  and  $8.990 \cdot 10^{-6} \text{ K}^{-1}$  giving a relative error of 0.4%. As mentioned previously, this should be seen as an estimate of reachable precision. The lengths of both fibers are measured to be 1.13 m and 1.19 m respectively.

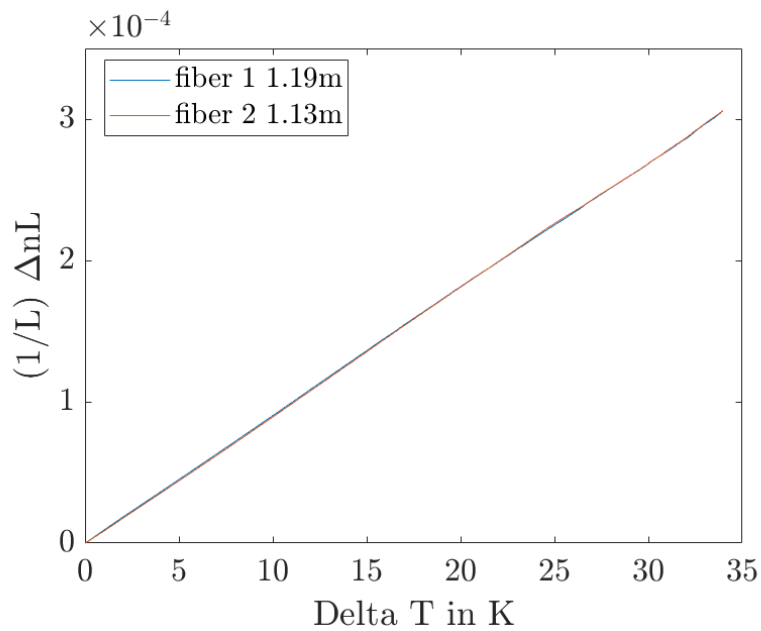


Figure 21: Measurement of the optical path change of two acrylate fibers with increasing temperature

Comparing with the result obtained with the 4.65 m long single acrylate fiber, no significant deviation is observed. Thus we conclude that interpolation of the temperature data with time is a sufficient tool to convert intensity data as a function of time to intensity data as a function of temperature and corrects sufficiently for smaller nonlinearities. Initial concerns regarding nonlinear temperature increase turned out to be unjustified. The advantage of having data with higher frequency components and thus clearer separation from noise outweigh the disadvantages. This justifies the use of a fast ramping process throughout the course of the subsequent experiments. It should be noted that nonlinearities lead to broadening of the signal in the frequency spectrum so that they do become an issue in the filtering process when too large.

From the cooling process a thermal sensitivity of  $9.1464 \cdot 10^{-6} \text{ K}^{-1}$  was obtained. Analysis of data extracted from cooling processes is generally more noisy and nonlinear so that a larger variance is expected as observed here.

Three successful experiments with an aluminum and an acrylate fiber were carried out. Here, it was confirmed that measuring the ratio gives a lower standard deviation than considering absolute values. Two measurements taken on the same day gave a relative

difference on the absolute value of 3% with a relative difference of the ratio of the thermal sensitivity of both fibers of 0.1%. Considering all three measurements we obtain 2% and 0.4% respectively. In conclusion, we choose to measure all fibers with a reference fiber of comparable lengths whenever possible. The single acrylate fiber and the aluminum fiber here were measured to have a length of 1.15 m and 1.25 m respectively.

As the dual acrylate fiber had a length of 12.9 m while the longest available acrylate fiber had a length of 4.90 m these are the lengths chosen for comparison of the dual acrylate and acrylate fiber. Three successful experiments with the reference fiber were carried out.

Measurements with the copper fiber were challenging due to increasingly worse thermal insulation and resulting irregularities. Four acceptable measurements were carried out. The fibers were measured to have a length of 2.85 m and 3.08 m.

Experimental fiber	Ratio
Aluminum	$1.877 \pm 0.007$
Copper	$1.533 \pm 0.015$
Dual Acrylate	$1.14 \pm 0.02$

Table 7: Ratios of the thermal sensitivity of Aluminum, Copper and Dual Acrylate coated optical fibers to the thermal sensitivity of the Acrylate coated fiber with uncertainties

The ratios of the thermal sensitivity of the aluminum, dual acrylate and the copper fiber with error bars are presented in figure 22 with relative errors of 0.4%, 1% and 2% and are further given in table 7.

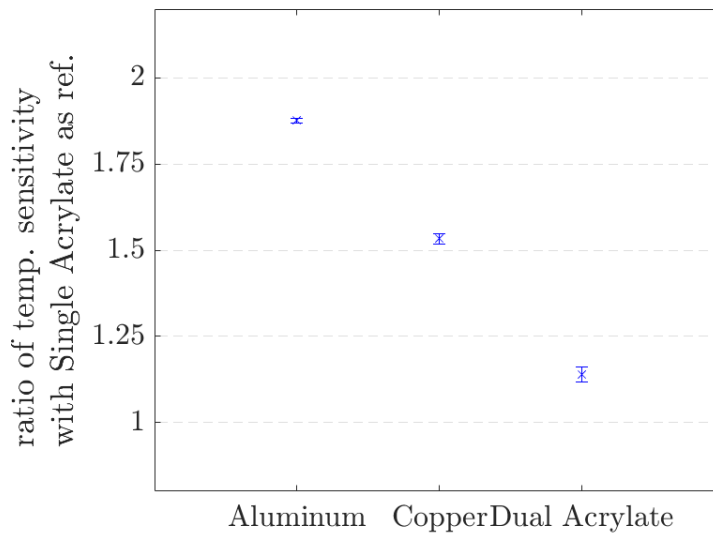


Figure 22: Ratios of the thermal sensitivity of Aluminum, Copper and Dual Acrylate coated optical fibers to the thermal sensitivity of the Acrylate coated fiber acting as a reference throughout the course of these experiments

Throughout the course of these experiments intensity was recorded during cooling and evaluated when possible. In total, five experimental runs including the initial runs with only acrylate fibers with evaluable heating and cooling were recorded. From those ex-

periments only the thermal sensitivity of the acrylate fiber were measured to be  $9.3 \pm 0.4 \cdot 10^{-6} \text{ K}^{-1}$  and  $9.5 \pm 0.6 \cdot 10^{-6} \text{ K}^{-1}$  for the heating and cooling process respectively. In conclusion they are not statistically different from each other.

Multiple attempts were carried out to measure the bare fiber with a reference but had to be given upon due to the high sensitivity of the bare fiber. However, it was possible to obtain a measurement of the bare fiber without a reference. The length of the bare fiber used was 93 cm. The optical path length change as a function of temperature for all fibers measured is presented in figure 23.

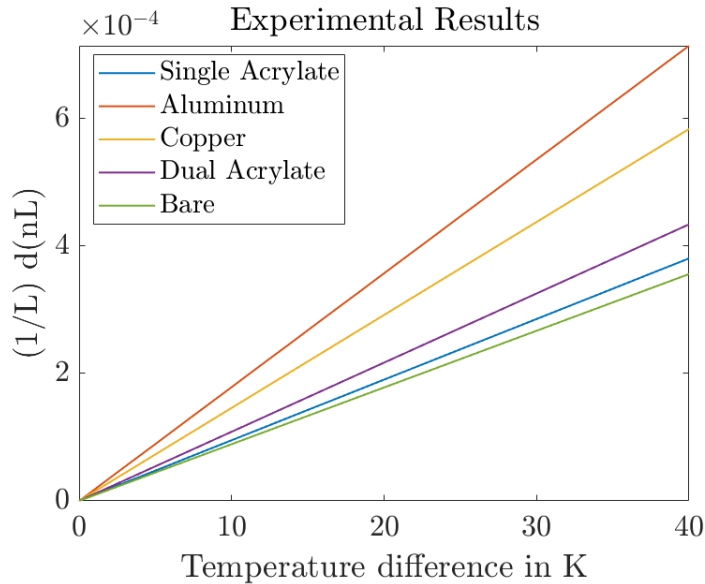


Figure 23: Measured Optical path change with temperature of coated and bare fiber

Absolute values for the thermal sensitivity of these fibers are obtained by multiplying the obtained ratios with the mean of all measured values for the single acrylate fiber which resulted to be  $(9.5 \pm 0.2) \cdot 10^{-6} \text{ K}^{-1}$ .

The error is obtained by error propagation of the statistical errors on the mean of the single acrylate fiber and the standard deviation on the ratio.

The results are presented in figure 24 plotted in blue alongside theoretical results from simulations and analytic results and are further presented in table 8. Good agreement between calculated and measured results is observed for acrylate, aluminum and dual acrylate. The agreement for acrylate and aluminum is especially good. At the same time these fibers have the highest difference in thermal response with a ratio of 1.88. A deviation of two standard deviations is observed between the measured and analytic result of the bare fiber. The larger error is likely caused by an increased sensitivity to environmental noise. Analytic results for the Copper fiber agree with the simulation. However, measurements are significantly lower. The reason is believed to lie in the experimental difficulties experienced for measurements with the copper coated fiber and as pointed out previously accurate modelling of the effects of the carbon layer was difficult (see section 4.4).

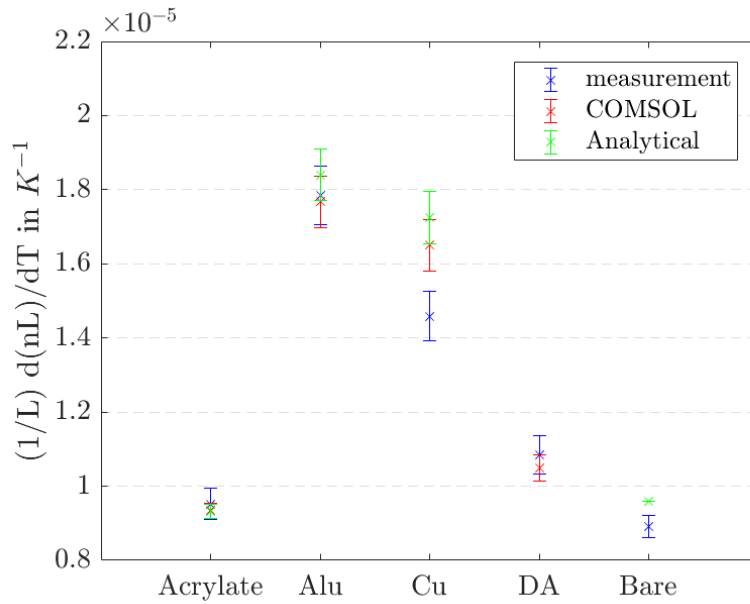


Figure 24: Absolute thermal sensitivity of analyzed coated fibers as derived experimentally in comparisons with the results from the Simulation and analytic calculations

Fiber	Exp.	COMSOL	Analytic
Acrylate	$(9.5 \pm 0.4) \cdot 10^{-6} \text{ K}^{-1}$	$(9.3 \pm 0.2) \cdot 10^{-6} \text{ K}^{-1}$	$(9.3 \pm 0.2) \cdot 10^{-6} \text{ K}^{-1}$
Aluminum	$(17.8 \pm 0.8) \cdot 10^{-6} \text{ K}^{-1}$	$(17.7 \pm 0.7) \cdot 10^{-6} \text{ K}^{-1}$	$(18.4 \pm 0.7) \cdot 10^{-6} \text{ K}^{-1}$
Copper	$(14.6 \pm 0.3) \cdot 10^{-6} \text{ K}^{-1}$	$(16.5 \pm 0.7) \cdot 10^{-6} \text{ K}^{-1}$	$(17.3 \pm 0.7) \cdot 10^{-6} \text{ K}^{-1}$
Dual Acrylate	$(10.8 \pm 0.5) \cdot 10^{-6} \text{ K}^{-1}$	$(10.5 \pm 0.4) \cdot 10^{-6} \text{ K}^{-1}$	-
Bare	$(8.9 \pm 0.3) \cdot 10^{-6} \text{ K}^{-1}$	-	$9.6 \cdot 10^{-6} \text{ K}^{-1}$

Table 8: Absolute thermal sensitivity of analyzed coated fibers as derived experimentally in comparisons with the results from the Simulation and analytic calculations

### 6.3 Discussion

A first point of discussion should be the precision at which measurements could be carried out. Precision on absolute values of thermal sensitivity was a few percent and thus relatively low. As error sources we suspect irregularities in the heating process and the large error on the length of the fibers. Irregularities in the heating process could be studied and remedied by using multiple temperature sensors to get a good idea of the heat distribution as a function of time and add insulation/adjust the heat plate as necessary. The length of the fibers could only be measured to cm precision with a folding ruler which does correspond to an error in the percentage range. Further, the way the fiber

was launched into the box, bumping the heat box, which can happen during realignment between measurements, changes the amount of fiber inside the box. As another problem was decreasing insulation due to the way the fiber was launched into the box, this should be done differently in future experiments.

In single cases re-cleaving between measurements was necessary and while the length of the cut off fiber end was measured this could lead to further uncertainties. Systems to measure the fiber length with mm precision are commercially available reducing the error on length by an order of magnitude. Furthermore, as the final set up deals with much longer fibers, measuring the fiber length by scanning the laser and counting fringes might give a better resolution. With improvements and increased caution on the lengths measurements of the fibers it is deemed feasible to reduce the error on the temperature sensitivity ratio from 0.4% to the target value of 0.1%.

As measurements for the aluminum coated fiber where in good agreement with the simulation and theory, the estimation of the thermal sensitivity of the suggested custom made fiber with a reduced cladding of  $80\ \mu\text{m}$  and a coating radius of  $250\ \mu\text{m}$  is deemed to be very plausible to be accurate. This gives a possibility to decrease the length of the short arm of the fiber interferometer reducing the delay and thus the conditions on the prestabilized frequency noise spectrum making this method viable for a larger range of lasers. Alternatively, the length of the long arm of the FI can be increased yielding a better short-term stability in applications where this is necessary.

Lastly, it should be mentioned that throughout the thesis the coefficient of thermal expansion as well as the thermo-optic coefficient are approximated to be constant while in fact they are themselves functions of temperature. However, they show a neglectable dependency around room temperature. Further the temperature dependency of the TOC will not effect measurements regarding the ratio as the cores of the fibers are the same.

In summary, the experiments carried out found the single coated acrylate fiber and the aluminum fiber to be a suitable option for the suggested drift-free FI and the required precision is assessed as feasible given improvements to the length measurement of the optical fibers.

## 7 Outlook

This work is concluded by the suggestion of a drift-free fiber interferometer for laser frequency stabilization using metal coated fibers. The set up is depicted in figure 25. A list of components with their suppliers can be found in the Appendix (section 8). As mentioned previously, a laser has been ordered with a frequency noise spectrum that flattens out around 100 kHz. Fast feedback and frequency control is possible via an EOM that is integrated for this purpose in the laser cavity. An optical isolator is further included.

Cutting the fibers to the correct length with a high precision will be a crucial part of the work in setting-up the fiber interferometer. As thicknesses of coatings vary due to the manufacturing process, values derived here are a good approximation but derivations should be expected so that it is necessary to measure the ratio of the thermal sensitivity with the for the FI intended fibers. With an increased length and an improved length measurement the required precision can be reached using the experimental method described in this thesis. The configuration of the fibers should correspond as closely as possible to their final configuration when in use for laser stabilization. This includes the

coiling of the fibers as well as the isolation.

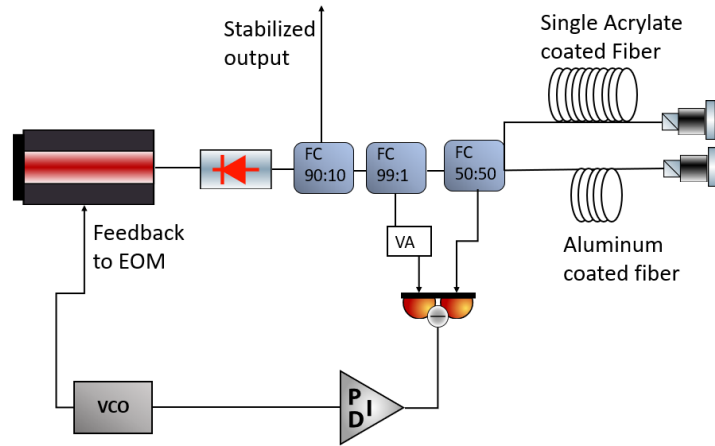


Figure 25: Suggested Design for long-term frequency stabilization with  $L_1 = 20$  m,  $L_2 = 37.6$  m . 90% of the laser output power are available for experiments as stabilized output. 10% of the power are used for the stabilization. The lengths of the arms of the MI are chosen according to the measured ratio of 1.877. The optical path difference is chosen as 35.2m allowing to reach a few kHz short-term stability comfortably as analyzed in section 2.2. The interference signal is picked of twice, at the 50/50 beam splitter and the 99/1 beam splitter and both signals are subtracted from each other using a balanced detector. Intensity differences can be corrected for using the electrically controlled variable attenuator. The electronic feedback loop consists of a proportional–integral–derivative controller (PID) and a voltage controlled oscillator (VCO) and feedback is provided by an EOM in the laser cavity.

Regarding the isolation there is a consensus in the reviewed literature that the best results are achieved by combining two or more boxes. The inner box is made out of aluminum and additionally it seems of advantage to place the fiber interferometer inside in a ring-shaped aluminum box (see section 2.2). The outer box serves acousto-isolation as well as additional isolation against thermal fluctuations and vibrations. For this purpose a Styrofoam box can be used with additional insulation material between both boxes.

Future work could further focus on increasing the wavelength range of operation. Additionally, the analysis and design of fibers with different thermal sensitivities is an active field of research. On a longer time scale and without an immediate application in mind, it will be interesting to study different core materials and their properties thoroughly. Few options have proven reliable single-mode operation thus far and even fewer once are commercially available so that this would provide an interesting prospect for more fundamental research. The aim would be to find fibers with a higher ratio of thermal sensitivity.

In summary, the suggested design is a solution for the problem of a portable laser source with suitable properties for Ultrasound Optical Tomography so that this medical imaging technique is brought one step closer to the development of a prototype that can be used in a hospital.

## References

- [1] Davies, N. and Oxford University Press. *Europe: A History*. Pimlico (Series). Oxford University Press, 1996. ISBN: 9780198201717.
- [2] New York Times. *Developer of the Laser Calls It ‘A Solution Seeking a Problem’; President of Korad Spends Spare Time Gardening and Fixing TV Sets*. 1964. URL: <https://www.nytimes.com/1964/05/06/archives/developer-of-the-laser-calls-it-a-solution-seeking-a-problem.html>.
- [3] N. Hinkley et al. “An Atomic Clock with 10<sup>-18</sup> Instability”. In: *Science* 341.6151 (2013), pp. 1215–1218. DOI: 10.1126/science.1240420.
- [4] S. A. Diddams et al. “Standards of Time and Frequency at the Outset of the 21st Century”. In: *Science* 306.5700 (2004), pp. 1318–1324. DOI: 10.1126/science.1102330.
- [5] J. L. Hall. *Frequency-stabilized lasers: a parochial review*. 1993. DOI: 10.1117/12.143668. URL: <https://doi.org/10.1117/12.143668>.
- [6] D. R. Leibrandt et al. “Spherical reference cavities for frequency stabilization of lasers in non-laboratory environments”. In: *Opt. Express* 19.4 (Feb. 2011), pp. 3471–3482. DOI: 10.1364/OE.19.003471.
- [7] H. Jiang. “Development of ultra-stable laser sources and long-distance optical link via telecommunication networks”. PhD thesis. Université Paris-Nord-Paris XIII, 2010.
- [8] J. Kong et al. “Long-term laser frequency stabilization using fiber interferometers”. In: *Review of Scientific Instruments* 86.7 (2015), p. 073104. DOI: 10.1063/1.4926345.
- [9] B. Lee. “Review of the present status of optical fiber sensors”. In: *Optical Fiber Technology* 9.2 (2003), pp. 57–79. ISSN: 1068-5200.
- [10] L. Perret, P. Pfeiffer, and A. Chakari. *Influence of non-linearities in wavelength-swept absolute distance interferometry*. 2007. DOI: 10.1117/12.726025.
- [11] A. Walther et al. “Analysis of the potential for non-invasive imaging of oxygenation at heart depth, using ultrasound optical tomography (UOT) or photo-acoustic tomography (PAT)”. In: *Biomedical Optics Express* 8.10 (2017), pp. 4523–4536. ISSN: 2156-7085. DOI: 10.1364/B0E.8.004523.
- [12] A. Kinos et al. “Development and characterization of high suppression and high &#x00E9;tendue narrowband spectral filters”. In: *Appl. Opt.* 55.36 (Dec. 2016), pp. 10442–10448. DOI: 10.1364/A0.55.010442. URL: <http://ao.osa.org/abstract.cfm?URI=ao-55-36-10442>.
- [13] W. Moerner et al. *Persistent Spectral Hole-Burning: Science and Applications*. Topics in Current Physics. Springer Berlin Heidelberg, 2012. ISBN: 9783642832901.
- [14] P. Hofmann. *Solid State Physics: An Introduction*. Physics textbook. Wiley, 2011. ISBN: 9783527657070.

- [15] Y. T. Chen. “Use of single-mode optical fiber in the stabilization of laser frequency”. In: *Appl. Opt.* 28.11 (June 1989), pp. 2017–2021. DOI: 10.1364/AO.28.002017.
- [16] B. Saleh and M. Teich. *Fundamentals of Photonics*. Wiley Series in Pure and Applied Optics. Wiley, 2013. ISBN: 9781118585818.
- [17] W.-K. Lee et al. “Linewidth reduction of a distributed-feedback diode laser using an all-fiber interferometer with short path imbalance”. In: *Review of Scientific Instruments* 82.7 (2011), p. 073105. DOI: 10.1063/1.3606439.
- [18] F. Kéfélian et al. “Ultralow-frequency-noise stabilization of a laser by locking to an optical fiber-delay line”. In: *Opt. Lett.* 34.7 (Apr. 2009), pp. 914–916. DOI: 10.1364/OL.34.000914.
- [19] D. Li et al. “Efficient laser noise reduction method via actively stabilized optical delay line”. In: *Opt. Express* 25.8 (Apr. 2017), pp. 9071–9077. DOI: 10.1364/OE.25.009071.
- [20] Lintz et al. *Dual, feed-forward + feed-back laser frequency control for efficient and convenient diode laser line narrowing*. 2017. DOI: 10.1117/12.2296158.
- [21] Smid et al. “Frequency noise suppression of a single mode laser with an unbalanced fiber interferometer for subnanometer interferometry”. In: *Sensors* 15.1 (2015), pp. 1342–1353. DOI: 10.3390/s150101342.
- [22] Y. Li et al. “Metal coating of fiber Bragg grating and the temperature sensing character after metallization”. In: *Optical Fiber Technology* 15.4 (2009), pp. 391–397. DOI: 10.1016/j.yofte.2009.05.001.
- [23] P. Hobbs. *Building Electro-Optical Systems: Making It all Work*. Wiley Series in Pure and Applied Optics. Wiley, 2011. ISBN: 9781118211090.
- [24] P. C. D. Hobbs. “Ultrasensitive laser measurements without tears”. In: *Appl. Opt.* 36.4 (Feb. 1997), pp. 903–920. DOI: 10.1364/AO.36.000903.
- [25] L. Rippe. “Personal comment”. 2019.
- [26] Fiber Resources. *Product Name: 1550 nm Low Wavelength and Temperature Dependent Faraday Mirror*. 2019. URL: [http://www.fiber-resources.com/1550-nm-Low-Wavelength-and-Temperature-Dependent-Faraday-Mirror\\_p207.html](http://www.fiber-resources.com/1550-nm-Low-Wavelength-and-Temperature-Dependent-Faraday-Mirror_p207.html).
- [27] W. Wu et al. “Open-loop fiber-optic gyroscope with a double sensitivity employing a polarization splitter and Faraday rotator mirror”. In: *Opt. Lett.* 43.23 (Dec. 2018), pp. 5861–5864. DOI: 10.1364/OL.43.005861.
- [28] M Squared. *SolsTiS frequency noise*. 2019. URL: <http://www.m2lasers.com/solstis.html>.
- [29] Schäfter + Kirchhoff. *Fiber Cables*. 2019. URL: <https://www.sukhamburg.com/download/FiberCables.pdf>.

- [30] *Aluminum: Properties and Physical Metallurgy*. Aluminum / J.E. Hatch Hrsg. American Society for Metals. American Society for Metals, 1984. ISBN: 9780871701763.
- [31] J. Davis and A. Committee. *Copper and Copper Alloys*. ASM specialty handbook. ASM International, 2001. ISBN: 9780871707260.
- [32] S.-T. Shiue and W.-H. Lee.  
“Thermal stresses in carbon-coated optical fibers at low temperature”.  
In: *Journal of Materials Research* 12.9 (1997), pp. 2493–2498.  
DOI: 10.1557/JMR.1997.0329.
- [33] H. Olson. “Mechanical and Optical Behaviour of A Novel Optical Fiber Crack Sensor and An Interferometric Strain Sensor”.  
PhD thesis. Massachusetts Institute of Technology, 2002.
- [34] Y. P. Michel et al. “Mechanical characterisation of the four most used coating materials for optical fibres”. In: *2015 International Conference on Photonics, Optics and Laser Technology (PHOTOPTICS)*. Vol. 1. Mar. 2015, pp. 91–95.
- [35] A. Mitra et al. *Thermal stability of the CPC Fiber Coating System*. WP4250. Corning Incorporated, 2010.
- [36] N. Lagakos, J. A. Bucaro, and J. Jarzynski.  
“Temperature-induced optical phase shifts in fibers”.  
In: *Appl. Opt.* 20.13 (July 1981), pp. 2305–2308. DOI: 10.1364/AO.20.002305.
- [37] S.-T. Shiue and Y.-S. Lin. “Thermal stresses in metal-coated optical fibers”.  
In: *Journal of applied physics* 83.11 (1998), pp. 5719–5723.  
DOI: 10.1063/1.367427.
- [38] Advanced Fiber Tools GmbH. *Single-Mode Fiber*. 2019.  
URL: <https://www.advanced-fiber-tools.de/pdf/singlemodefibers.pdf>.
- [39] S. Wilson. “Temperature sensitivity of optical fibre path length”.  
In: *Optics Communications* 71.6 (1989), pp. 345–350.  
DOI: 10.1016/0030-4018(89)90046-1.
- [40] H. Li et al. “Thermal sensitivity of tellurite and germanate optical fibers”.  
In: *Opt. Express* 15.14 (July 2007), pp. 8857–8863. DOI: 10.1364/OE.15.008857.  
URL: <http://www.opticsexpress.org/abstract.cfm?URI=oe-15-14-8857>.
- [41] A. Kinos. “Light-Matter Interaction and Quantum Computing in Rare-Earth-Ion-Doped Crystals”. PhD thesis. Atomic Physics, Feb. 2018.  
ISBN: 978-91-7753-543-0.
- [42] NIST. *Analysis of Time Domain Data*. 2019.  
URL: <https://tf.nist.gov/phase/Properties/four.htm>.
- [43] D. W. Allan. *Clock characterization tutorial*.  
National Aeronautics and Space Administration, Office of Management, 1983.
- [44] Iowa State University. *Allan Variance*. 2019.  
URL: <http://home.engineering.iastate.edu/~shermanp/AERE432/lectures/Rate%20Gyros/Allan%20variance.pdf>.

- [45] J. L. Hall. “Stabilizing Lasers for Applications in Quantum Optics”.  
In: *Quantum Optics IV*. Ed. by J. D. Harvey and D. F. Walls.  
Berlin, Heidelberg: Springer Berlin Heidelberg, 1986, pp. 273–284.  
ISBN: 978-3-642-71407-8.
- [46] S. Bennetts et al. “External cavity diode lasers with 5kHz linewidth and 200nm tuning range at 1.55 $\mu$ m and methods for linewidth measurement”.  
In: *Opt. Express* 22.9 (May 2014), pp. 10642–10654. DOI: 10.1364/OE.22.010642.
- [47] M. Bass et al. *Handbook of Optics, Third Edition Volume II: Design, Fabrication and Testing, Sources and Detectors, Radiometry and Photometry*. 3rd ed.  
New York, NY, USA: McGraw-Hill, Inc., 2010. ISBN: 9780071498906.
- [48] J.-R. Lee, D. Dhital, and D.-J. Yoon. “Investigation of cladding and coating stripping methods for specialty optical fibers”.  
In: *Optics and Lasers in Engineering* 49.3 (2011), pp. 324–330. ISSN: 0143-8166.

## 8 Appendix

### Linewidth, Frequency Spectrum and Allan Deviation

Commonly, the stability of a laser is described by the linewidth giving an estimate of the output's frequency spectrum. However, this description has little implication about the frequency noise spectrum, crucial especially for stabilized lasers. This is illustrated well when looking at specifications provided by the manufacturer where a different linewidth is measured for different time intervals.

There are different types of noise playing a role in the frequency output of a laser such as white noise, white frequency noise and flicker frequency noise. The latter lead to a steady increase of the standard deviation with number of sample points making it an unsuitable statistical description [42]. Instead, new statistical tools were developed for the field of laser stabilization. The standard deviation is thus replaced with the more suited M-sample variance:

$$\sigma_y^2(M, T, \tau) = \frac{1}{M-1} \left[ \sum_{i=0}^{M-1} \left[ \frac{x(iT + \tau) - x(iT)}{\tau} \right]^2 - \frac{1}{M} \left[ \sum_{i=0}^{M-1} \frac{x(iT + \tau) - x(iT)}{\tau} \right]^2 \right] \quad (31)$$

$$= \frac{1}{M-1} \left[ \sum_{i=0}^{M-1} \bar{y}_i^2 - \frac{1}{M} \left[ \sum_{i=0}^{M-1} \bar{y}_i \right]^2 \right] \quad (32)$$

where  $\tau$  gives measuring intervals,  $M$  the number of samples and  $T$  is the time between each frequency sample [42]. The Allan variance, named after David W. Allan a pioneer in the area of laser stabilization, is then subsequently defined as

$$\sigma_y^2(\tau) = \langle \sigma_y^2(1, \tau, \tau) \rangle \quad (33)$$

$$= \frac{1}{2} \langle (y_{n+1}^- - y_n^-)^2 \rangle \quad (34)$$

$$= \frac{1}{2\tau^2} \langle (x_{n+2} - 2x_{n+1} + x_n)^2 \rangle \quad (35)$$

The Allan variance is further related to the frequency noise spectrum by integration. Note that the Allan variance is a function of the time of measurement intervals  $\tau$  meaning it is presented by a function rather than a single number or at least given with the corresponding  $\tau$  [43].

It is further important to note, that drift is given as a low frequency noise and presented in a frequency noise spectrum while both Allan variance and a spectral linewidth are designed to reflect statistical errors, not systematical errors accumulating with time [44]. Discussion about short-term stability and long-term stability should thus be clearly differentiated and is not to be confused. Quantities given are to be interpreted with a mathematical understanding of the principles presented here and with their resulting limitations on information they yield.

### Technical discussion on Control Bandwidth

An important parameter in characterizing a feedback system is the unity gain frequency, it is the highest frequency for which noise is reduced. In the case of laser frequency

stabilization this frequency is dictated by the delay of the system. In order to suppress noise instead of amplifying it the phase given by the product of angular frequency  $\omega$  and delay time  $\tau$  can not exceed  $90^\circ$  imposing the condition  $\omega \cdot \tau < \frac{\pi}{2}$  [45].

In order to stabilize a laser efficiently the control bandwidth of the system must be high enough such that the servo gain provided by the stabilization system will either match or better exceed the rise of the noise at low frequencies. A noise frequency spectrum can often be provided by the manufacturer upon request. A frequency spectrum resulting of a stabilization system that can not match the rise of noise at low frequencies is characterized by a sharp peak in the middle and broader peaks at higher frequencies instead of just one centered peak. When only the linewidth is given, this can not identified (see 26).

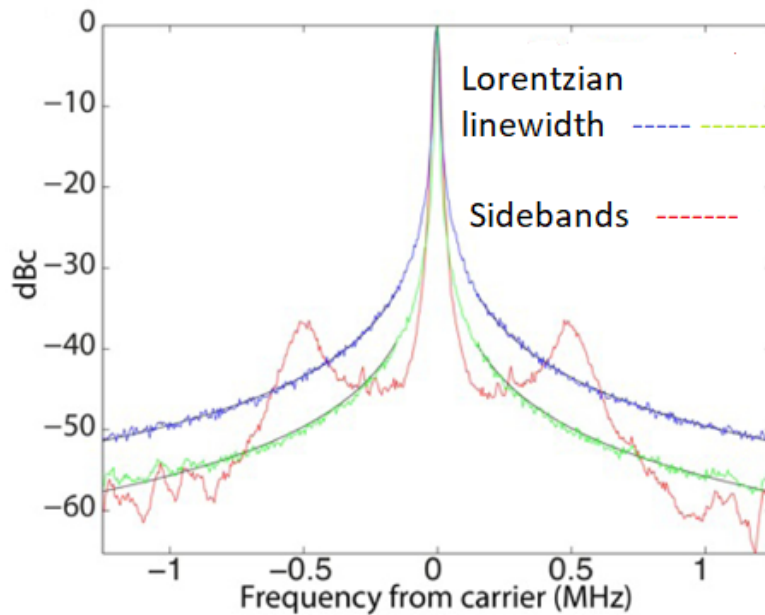


Figure 26: Examples of stabilized laser linewidth with and without sidebands. In blue and green we see a lorentzian linewidth indicating a high enough unity gain frequency and thus sufficient gain at high frequencies. In red we see a linewidth with sidebands as the gain at those frequencies is too low indicating a low unity gain frequency [46]

Any delays in response time will decrease the control bandwidth of a system. However, restrictions on how steep the slope of the gain can be also apply: more than a slope of  $1/1.5$  on a log-log scale has a negative impact on the functionality of a stabilization system [47]. In principle, a high enough gain can reduce the intrinsic noise of a laser to any desired small value. This does however require pushing up the unity gain frequency as limitations to the slope steepness apply and thus impose increasing limitations on the allowed delay.

Let us consider our example of a 20 m long short arm in a Michelson set up giving an additional delay of 193 ns. Other delays are estimated from the detector bandwidth ( $\approx 15$  MHz) and delays in the cables with an assumed total length of 2 – 3 meters and a propagation speed corresponding to 70% of the speed of light which yields  $\approx 100$  ns. A conservative estimate of the achievable gain with a slope of -1 is presented in figure 27. From this graph we estimate a unity gain frequency of 550 kHz.

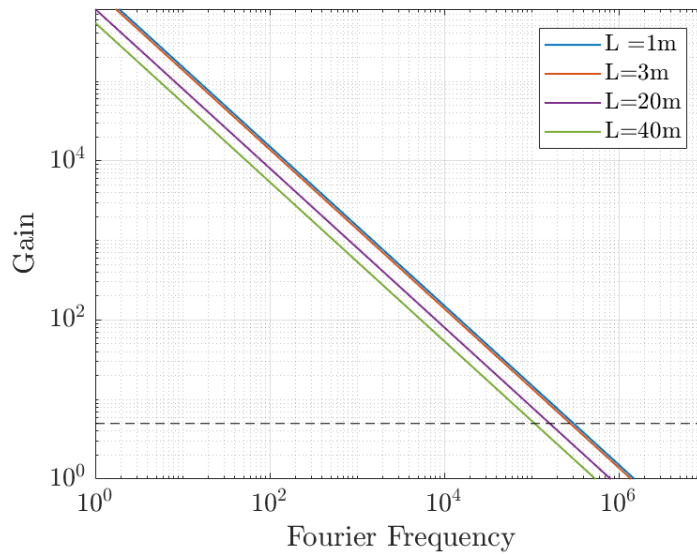


Figure 27: Analysis regarding unity gain frequencies for a given delay length

## Bending losses

Bending losses for the Aluminum fiber were tested by measuring the power after the fiber with a straight fiber and a coiled fiber with a radius of 3 cm. This was carried out 10 times iteratively. Results of these measurements are presented in figure 28.

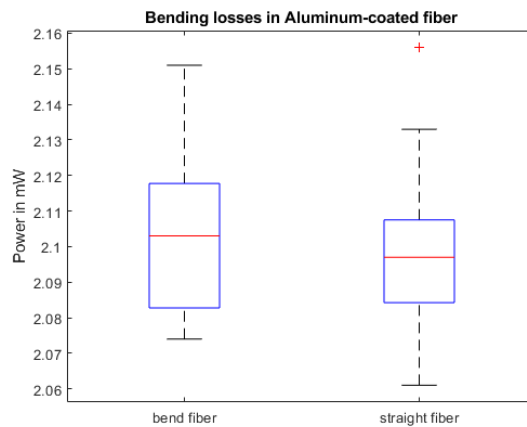


Figure 28: Experimental comparison of the output power of a 1m-Aluminum fiber at a wavelength of 690 nm

## Analytic Formulas for Thermal Stress in Metal Coated Fibers

The following formulas are given as presented in the paper "Thermal stresses in metal-coated optical fibers" by Shiue et al..

$$\sigma_r = \left[ 1 + \gamma \frac{\delta + \mu}{\xi\delta - \mu\gamma} \right] \frac{\Delta\alpha\Delta T}{\delta} \quad (36)$$

$$\sigma_z = -\frac{\delta + \mu}{\xi\delta - \mu\gamma} \Delta\alpha\Delta T \quad (37)$$

$$k = \sqrt{(2\pi r_0) \frac{\xi\delta - \mu\gamma}{\delta\kappa}} \quad (38)$$

$$\xi = \frac{1}{\pi E_0 r_0^2} + \frac{1}{\pi E(r_1^2 - r_0^2)} \quad (39)$$

$$\kappa = \frac{3r_0}{4E_0} + \frac{r_0 [(r_0 + r_1)^2/4 - r_0^2 + 2(1 + \rho_1)r_1^2 \ln [(r_0 + r_1)/2r_0]]}{E_1(r_1^2 - r_0^2)} \quad (40)$$

$$\mu = \frac{2\rho_0}{E_0} + \frac{2\rho_1 r_0^2}{E_1(r_1^2 - r_0^2)} \quad (41)$$

$$\delta = \frac{1 - \rho_0}{E_0} + \frac{(1 - \rho_1)r_1}{E(r_1^2 - r_0^2)} \quad (42)$$

$$\gamma = \frac{\rho_0}{\pi E_0 r_0^2} + \frac{\rho_1}{\pi E_1(r_1^2 - r_0^2)} \quad (43)$$

where the index 0 indicates properties of the core and cladding and the index 1 indicates properties of the coating material and  $\Delta\alpha$  denotes the difference of CETs. Note that this equations hold for the core of the fiber where boundary effects can be neglected.

## Derivation of relation of phase $\varphi$ and optical path $nL$

$$T(\nu) = \tau_{max} / \left( 1 + \left( \frac{2\mathcal{F}}{\pi} \right)^2 \sin^2 \left( \frac{\pi\nu 2nL}{c} \right) \right) \quad \tau_{max} = 1 \quad (44)$$

$$T(\nu) = 1 / \left( 1 + \left( \frac{2\mathcal{F}}{\pi} \right)^2 \sin^2 \left( \frac{\pi\nu 2nL}{c} \right) \right) \quad \text{Taylor Expansion} \quad (45)$$

$$T(\nu) \approx 1 - \left( \frac{2\mathcal{F}}{\pi} \right)^2 \sin^2 \left( \frac{\pi\nu 2nL}{c} \right) \quad \sin^2(\Theta) = \frac{1 - \cos(2\Theta)}{2} \quad (46)$$

$$T(\nu) \approx 1 - \left( \frac{2\mathcal{F}}{\pi} \right)^2 \frac{1 - \cos \left( \frac{4\pi\nu nL}{c} \right)}{2} \quad (47)$$

$$T(\nu) \approx 1 - 2 \left( \frac{\mathcal{F}}{\pi} \right)^2 + 2 \left( \frac{\mathcal{F}}{\pi} \right)^2 \cos \left( \frac{4\pi\nu nL}{c} \right) \quad (48)$$

## Fiber Preparation

**Single and Dual Acrylate** While mechanical stripping of an acrylate coated fiber can be achieved, it was found that dipping the fiber in acetone beforehand reduced the risk of the fiber breaking in the process and the coating came off easier. The dual acrylate coating seemed to be more resistant than the acrylate coating and repetitive dipping in acetone and peeling was necessary.

**Aluminum Fiber** Stripping of the aluminum fiber was achieved with a water-based sodium hydroxide solution as suggested by Lee et al.[48]. While Lee et al. resolved the Aluminum coating in minutes with a NaOH solution with a concentration of 40% this could not be reproduced. I found that using a pre-mixed 50% solution from sigmaaldrich it was necessary to let the fiber soak overnight.



Figure 29: Chemical etching of the fiberguide Aluminum fiber with a 50% NaOH solution

Successful etching is easily identified by the formation of sodium aluminate according to the following chemical reaction:



It should be noted that skin contact with sodium hydroxide leads to severe chemical burns. Breathing in the fume of the solution presents a hazard as well so that work with this solvent should be carried out using a fume hood and appropriate precautions. Once etching is completed and the fiber is removed from the caustic soda solution it should be cleaned thoroughly.

**Copper Fiber** Removing copper coating of an optical fiber requires chemical etching as in the case of the aluminum coated fiber. The solvent used for copper is Iron(III) chloride. Dipping the end of the fiber in the solvent for twenty minutes was sufficient and the copper coating resolved entirely making the solvent increasingly darker as more copper is resolved in it. Iron(III) chloride is classified as corrosive and harmful. Upon completion of etching the fiber should be cleaned thoroughly.

**Bare Fiber** In order to have a fiber without any coating it was necessary to remove the coating of a one to two meter piece of single-acrylate coated fiber. This was achieved by letting the fiber soak in beaker filled with acetone for 2-3 days. While acetone is not the recommended solvent for single acrylate this worked rather well as the coating on the fiber seemed to swell and come off the fiber in one piece without resolving in the acetone so that after 2-3 days the optical fiber without coating as well as a string of acrylate coating could be retrieved. As the bare fiber is very sensitive extra care is required in handling it. Extensive contact with skin should further be avoided and gloves should be worn whenever possible.

## Validity of fiber length approximation

When determining the length of the optical fiber the piece outside of the heat box is neglected. The validity of this approximation was tested with a time-dependent COMSOL simulation. The ambient temperature is set as room temperature (293 K) and one end of the fiber piece outside the box is modeled as heat source with a temperature of 335 K. The time is chosen as one hour as this corresponds to the average heating time. Results are presented in the figure below and it can be easily seen that the temperature distribution can be approximated as a step function and no noticeable effect is observed on the fiber piece.

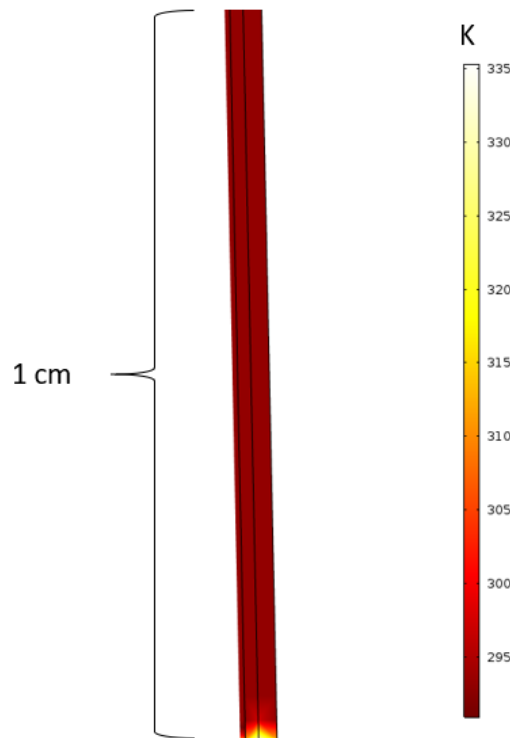


Figure 30: Validity of Fiber length Approximation: Pictured is 1cm of the modelled 10cm fiber piece outside of the box. As an approximation, the fiber piece was modelled to be entirely made of Aluminum. This gives an upper limit as Aluminum has the better thermal conductivity.

## Exemplary Results from frequency scanning the Laser

The possibility to scan the laser in frequency was frequently used to test the functionality of the set-up. Exemplary results of a laser scan are presented in figure 31. The intensity background without light was measured before and after the laser scan measurement. The average of background measurements was taken and subtracted from the signal. The signal was further divided by the reference.

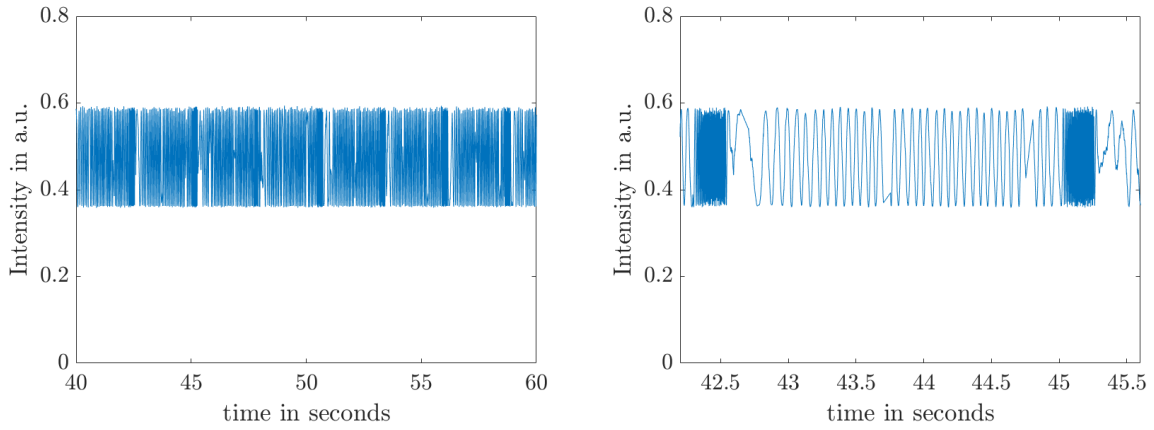


Figure 31: Detected fringes from scanning the laser 20 GHz mode hope free on a 4.65 m long fiber cavity. Note that the laser scans continously and scans back 10 times as fast. Left: Multiple scans over a time duration of 20 seconds Right: One scan over a time duration of a few seconds.

## Details of the Phase extraction in the Data Analysis

Extracting the phase can be achieved as follows: In a first step we take the Fourier transform of our data. The reader is reminded that the complex Fourier transform of a function in time is a function of frequency. This function is complex valued. The absolute value presents the amount of each frequency present in the transformed data. This becomes more obvious when we further look at the following relationships for the cosine and the sine function

$$\cos \omega t = \frac{1}{2}e^{i\omega t} + \frac{1}{2}e^{i(-\omega)t} \quad \sin \omega t = \frac{1}{2}ie^{i(-\omega)t} + \frac{1}{2}ie^{i(\omega)t} \quad (50)$$

This tells us that when writing cosine and sine with complex numbers as in the case of a Fourier transform they are represented by positive and negative frequencies, both contributing equally as it can be seen in figure 32.

From these considerations we can predict and understand the spectrum we obtain from our data; for now we will assume a perfect linearity between time and temperature. We expect to see two peaks corresponding to the same value of frequency, one on the positive x-axis, one on the negative x-axis with equal height after centering our data around 0. In addition we will further observe a DC-peak and potential additional peaks presenting noise at a given frequency. All essential information is contained in one set of frequencies, positive or negative, only. Filtering out only the positive frequencies and performing an inverse Fourier transform yields complex intensity data as a function of time and thus phase information for every measuring point.

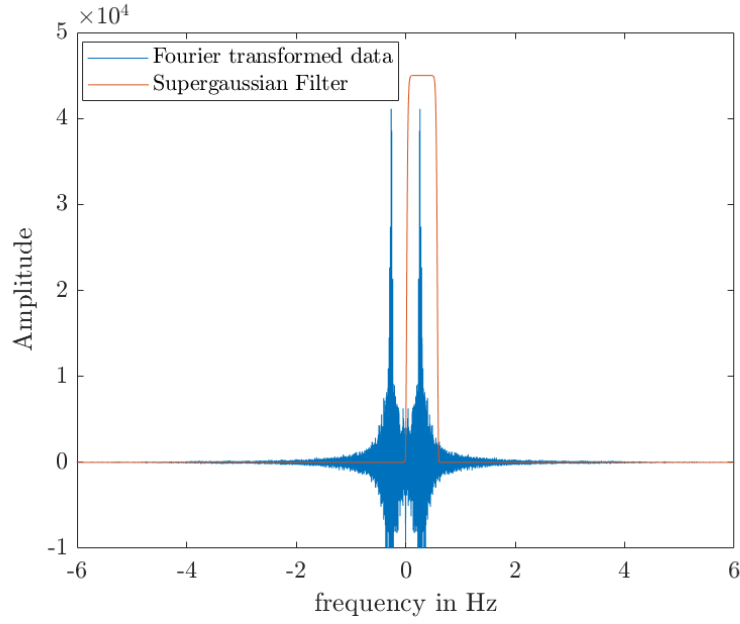


Figure 32: Example of Fourier transformed data from a 4.65 m single acrylate coated fiber with the temperature being ramped according to figure 15 left. The filter function chosen is a Supergaussian centered around 0.3 Hz with a FWHM of 0.2 Hz. The amplitude of the filter function is plotted as  $4.5 \cdot 10^4$  for illustration but set to 1 for all analytic purposes.

It is useful to use this step of filtering at the same time to filter out any noise as well as the DC-peak. As a filter function a higher order Gaussian function was used of the form

$$F(f) = \exp\left(-\left(\frac{(f - f_0)^2}{2\sigma^2}\right)^{10}\right) \quad (51)$$

which is further presented in figure 32.  $f_0$  denotes the central frequency and  $\sigma^2$  the variance. Note further that to conserve information on amplitude correctly, multiplication by a factor of two is necessary since one half of the amplitude is lost with the disregard of negative frequencies as it can easily be seen from equation 50.

After these steps each data point yielding the Intensity  $I$  at a time  $t$  is now given by  $I = re^{i\varphi}$  with the phase  $\varphi$  as given in equation 30. The original signal is obtained by plotting the real part as a function of time. Plotting the original signal as well as the real part of the signal after this transform is performed is further a useful check to see if the filters are chosen correctly i.e. no part of the signal is filtered out or to check for other obvious mistakes.

## List of Components

Component	Manufacturer	Price
Aluminum coated fiber	fiberguide AIS4.3/125 /175A	ca. 30 Euros/ meter
Acrylate coated fiber	Thorlabs, 630HP	5.30 Euros/ me- ter
Faraday Mirror	Thorlabs, custom made	ca. 1000 euros/ piece
Connectors	Newport	121 Euros/ piece
50/50 Coupler 2x2	Thorlabs, TW670R5P2	337.60 Euros
90/10 Coupler 2x1	Thorlabs, TW670R2A1	351,44 Euros
99/1 Coupler 2x1	Thorlabs, TW670R1P1	348.00 Euros
Electrically controlled variable fiber optic at- tenuator	OZ optics <a href="https://www.ozoptics.com/ALLNEW_PDF/DTS0010.pdf">https://www.ozoptics.com/ ALLNEW_PDF/DTS0010.pdf</a>	-
Balanced Photodetec- tor	Thorlabs, PDB440A	1335.10 Euros

Table 9: Component list